Università degli Studi di Padova
Dipartimento di Fisica ed Astronomia "Galileo Galilei"

Corso di Laurea in Fisica


# Feasibility study of a diagnostic wire calorimeter for the SPIDER experiment

**Laureando:**
Isabella Mario

Relatore: dottor Gianluigi Serianni
Correlatore: dottor Roberto Pasqualotto

Anno Accademico 2013/2014

*Ai miei genitori Patrizia e Maurizio,*
*Ai miei nonni Angelo e Mirella,*
*Ad Andrea e Riccardo,*
*A Leonardo.*

## Riassunto

Per ottimizzare il fascio di particelle per l'esperimento di fusione nucleare ITER è necessario misurare i parametri del fascio con un'alta risoluzione spaziale. Questo può essere fatto con un calorimetro diagnostico composto da una disposizione di fili in materiale idoneo. I fili, esposti al fascio, si scaldano a causa della deposizione di potenza e raggiungono una temperatura sufficientemente alta da irradiare la potenza termica ricevuta. La presente tesi mira al progetto preliminare di un calorimetro a fili di tungsteno per il fascio prodotto da SPIDER, il prototipo della sorgente del fascio per ITER. Il lavoro inizia con la simulazione dei risultati attesi per la calibrazione sperimentale della luce emessa da un campione di filo di tungsteno scaldato da una corrente elettrica e osservato da una telecamera. Successivamente saranno confrontate le misure e le simulazioni e il lavoro continua con la simulazione numerica dell'effetto di profili realistici per il fascio di SPIDER sul calorimetro a fili, deducendone i requisiti riguardo ai fili e alla loro distribuzione spaziale.

## Abstract

To optimise the particle beam for the nuclear fusion experiment ITER it is necessary to measure the beam parameters with high spatial resolution. This can be done with a diagnostic calorimeter composed of an arrangement of wires made of suitable material. The wires, exposed to the beam, heat up because of the deposition of power and reach a temperature high enough to irradiate the thermal power received. The present thesis aims at the preliminary design of a wire calorimeter made of tungsten for the beam produced in SPIDER, the prototype beam source for ITER. The work starts with the simulation of the results expected from the experimental calibration of the light emitted from tungsten wire samples heated by an electrical current and observed by a camera. After comparing measurements and simulations, the work continues with the numerical simulation of the effect on the calorimeter wires of realistic SPIDER beam profiles, deducing the requirements on the wires and on their spatial distribution.

# Contents

# Chapter 1

# Introduction

## 1.1 Energetical Problem

Energy is largely used in many everyday moments by billions people around the world; Most people worldwide have access to energy in differents parts of cities as public transports, homes and offices. Energy is produced by energy sources that are classified as fossil, like oil, coal and natural gas, and renewable, like solar, wind and hydroelectric energy sources. About hydroelectric and wind energy sources there are different disadvantages due to both the irregularity of the supply energy incomes and the location of production facilities. Solar energy source is widely used but it give a minor contribution with respect to other energy sources. The world huge energy demand has prompted the development of alternative solutions like controlled thermonuclear fusion as a cleaner energy source. The main goal of the international effort in the field of fusion energy, currently coordinated by IAEA, is to create an energy source, virtually, inexhaustible.

## 1.2 Fusion

To produce energy by fusing two atoms it is necessary that the difference in energy between final and initial status is positive: in a nuclear reaction the amount of energy released by a reaction is indicated with the Q-value . In the case of nuclear fusion two distinct nuclei join together to form a new type of atomic nucleus and if the Q-value of the reaction is positive energy is released: an example is the "proton-proton chain" (fig.1.1), that has a total Q-value of 26.73MeV, which is the main sequence of fusion in stars of the size of the Sun or smaller[26]. Another example is the fusion of deuterium with tritium that has a Q-value of 17.6MeV (fig.1.1):

$$D + T \rightarrow^4 He + n + 17.6MeV \tag{1.1}$$

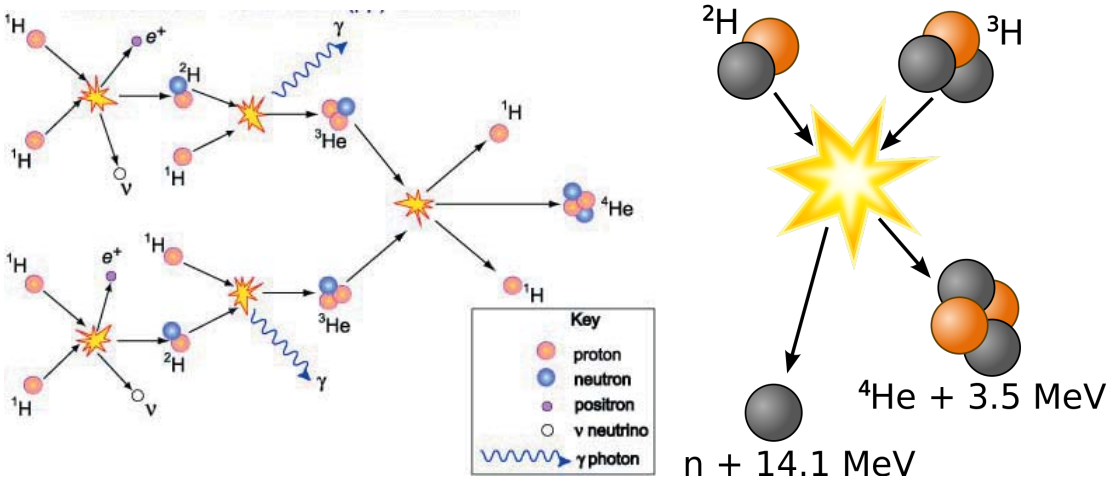


(a) *proton-proton chain.* (b) *D-T reaction.*

Figure 1.1: left: proton-proton chain; right: deuterium with tritium reaction

To merge two nuclei and obtain energy it is necessary to overcome the Coulomb barrier by bringing the nuclei close enough, then the electrostatic repulsion can be overcome by the attractive nuclear force, which is stronger at close distances: in order to make fusion possible it is therefore necessary that the nuclei have enough kinetic energy. Different fusion reactions can be used as "fuel" to termonuclear reactors (see fig.1.2)

| | | | |
|---|---|---|---|
| 1. | D + T | → | $^4$He (3.5 MeV) + n (14.1 MeV) |
| 2. | D + D | → | T (1.01 MeV) + p (3.02 MeV) (50%) |
| | | → | $^3$He (0.82 MeV) + n (2.45 MeV) (50%) |
| 3. | D + $^3$He | → | $^4$He (3.6 MeV) + p (14.7 MeV) |
| 4. | T +T | → | $^4$He + 2 n + 11.3 MeV |
| 5. | $^3$He + $^3$He | → | $^4$He + 2 p |
| 6. | $^3$He + T | → | $^4$He + p + n + 12.1 MeV (51%) |
| | | → | $^4$He (4.8 MeV) + D (9.5 MeV) (43%) |
| | | → | $^4$He (0.5 MeV) + n (1.9 MeV) + p (11.9 MeV) (6%) |
| 7. | D + $^6$Li | → | 2 $^4$He + 22.4 MeV |
| 8. | p + $^6$Li | → | $^4$He (1.7 MeV) + $^3$He ( 2.3 MeV) |
| 9. | $^3$He + $^6$Li | → | 2 $^4$He + p + 16.9 MeV |
| 10. | p + $^{11}$B | → | 3 $^4$He + 8.7 MeV |

Figure 1.2: list of the most favourable fusion reaction [20]

A realizable fusion reaction which has a high Q-value is between deuterium and tritium, since, as seen in fig.1.2[20], it has a high cross-section; moreover both Deuterium and Tritium can be found on Earth: the first is avaiable in seawater and the second is obtained from reaction:

$$n +^6 Li \rightarrow^4 He + T + 4.8MeV \tag{1.2}$$

In conclusion required nuclei used as "fuel" for fusion facilities are Lithium and Deuterium: both avaiable on Earth. There are several advantages of nuclear fusion with respect to fission[20]:

- its intrinsic safety due to the readiness of an eventual shutdown in case of anomalous conditions: the achievement and sustainment of physical conditions necessary for triggering fusion is so hard that, in case of necessity, it would be easy to stop;
- nuclear waste composed mostly of radioactive metallic structures of the fusion device and of the surrounding environment due to neutron activation have shorter lifetime than the nuclear waste produced in the fission facilities;

- it is possible to convert fusion energly directly to electricity through various methods like induction effects or electrostatic effects decelerating charged particles in an electric field;

However, to achieve fusion on Earth it is necessary to heat the fuel up to high temperature to give the particles enough kinetic energy to overcome coulombian barrier and begin the fusion process: this turns normal matter into plasma state.
Plasma is a state of matter and is formed when a gas is ionized and a non-negligible number of charge carriers (positive or negative ions/electrons) are locally separate in a globally neutral gas. Due to charge carriers, plasma behaves like a electrical conductor, e.g. responding to magnetic field. Particles in a plasma are not free because they are affected by each other's electrostatic field and this effect causes a collective behaviour. In a plasma electric field are shielded over a short distance called Debye's length $\lambda_D$ (eq.1.3):

$$\lambda_D = \sqrt{\frac{\epsilon_0 k_B T_e}{n e^2}} \tag{1.3}$$

where $T_e$ is electron temperature, $n$ electron density, $e$ electron charge, $k_B$ the Boltzmann constant and $\epsilon_0$ the permissivity of the vacuum.
In a fusion reactor the operating regime is obtained when output and input power are balanced: output power is mainly caused by two phenomena: transport and radiation (due to bremsstrahlung). The transposrt phenomenon is quantified by the so called energy confinement time $\tau_E$ (eq.1.4)[20]:

$$\tau_E = \frac{W}{P_L} \tag{1.4}$$

where $W$ is the total energy stored in a plasma and $P_L$ the power lost due to transport phenomena. The parameter that quantifies the ignition point is $nT\tau_e$ ($n$ density, $T$ temperature); by neglecting ignition regime and radiation eq.1.5 is obtained[20]:

$$n\tau_E = \frac{12T}{\langle \sigma v \rangle E_\alpha} \tag{1.5}$$

where $\sigma$ is the cross section(fig.1.3), $E_\alpha$ is the energy of $\alpha$-particle produced (e.g. 35MeV): the minimum of the $n\tau_E$ product corresponds to a temperature of $T = 25keV$, and for this temperature:

$$nT\tau_E > 5 \cdot 10^{21} keV m{-}3s \tag{1.6}$$

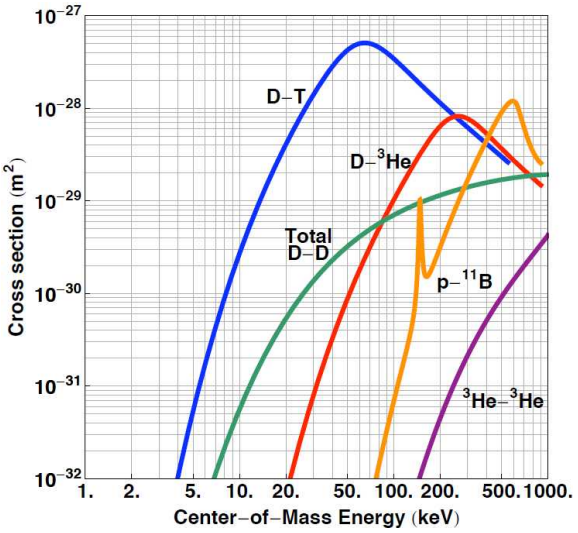


Figure 1.3: Fusion cross-sections of various fusion reactions as a function of kinetic energy of an incident D or p on a stationary target[20]

To increase the value of the triple product in eq.1.6 two thecniques are developed [20]:

- inertial confinement: to generate net fusion power by compressing to high densities a pellet of solid fusion fuel and by heating it to the temperature necessary for ignition. It is possible to generate fusion power before the sistem blows apart because the inertia keeps the fuel together for a finite time.

- magnetic confinement: due to the presence of charged particles a plasma responds to magnetic field that keeps it away from the material walls; various configurations are developed to magnetically confine plasma such as the thoroidal magnetic field with a poloidal component (to prevent charge separation): this configuration (mixing poloidal and toroidal components) is used in Tokamak and Stellarator configurations (see fig.1.4).

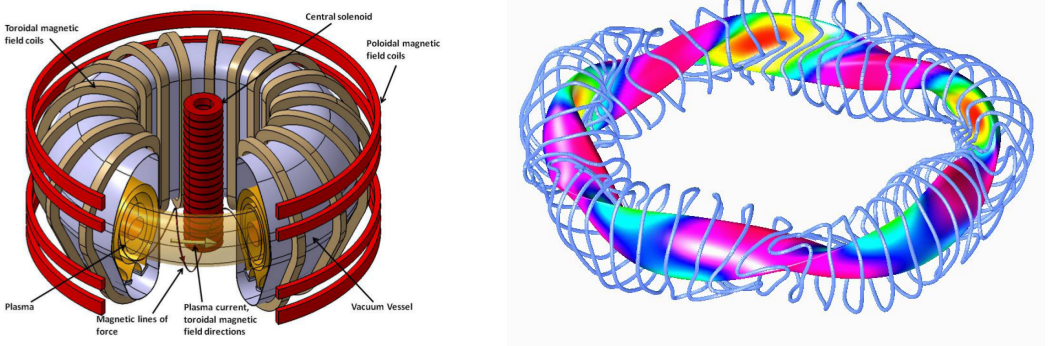


(a) *Tokamak.* (b) *Stellarator.*

Figure 1.4: Use of magnetic field with both toroidal and poloidal components: examples of facilities based on Tokamak configuration are EFDA-JET[1] in Great Britain and DIII-D[2]); large Stellarator ar LHD[3] in Japan and Wendelstein-7X[4] in Germany.

## 1.3 ITER

ITER represents the most advanced project on nuclear fusion; ITER facility (cutaway in fig.1.5) is under construction in Cadarache France and is funded by EU, USA, Russia, Japan, India, China and South Korea[20][17].

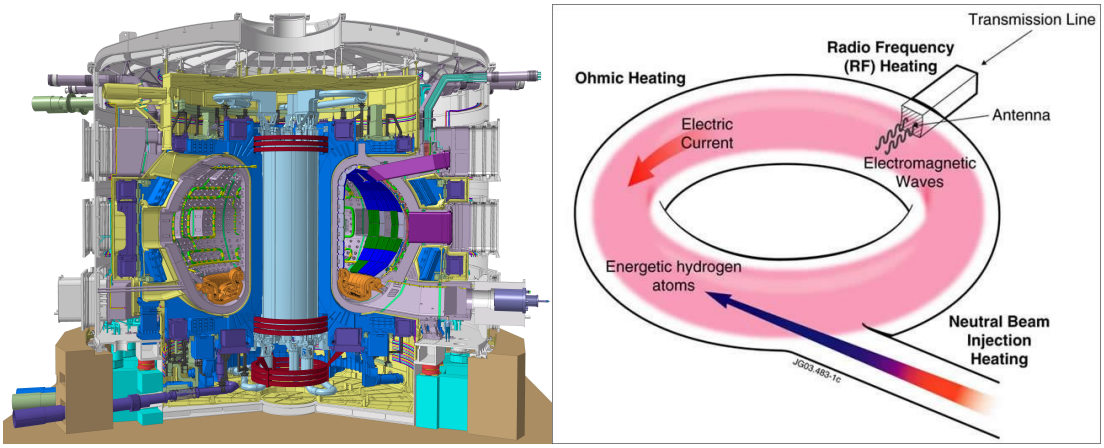


(a) *ITER facility.* (b) *Plasma Heating System.*

Figure 1.5: ITER cutaway view(left) and ITER heating system [17]

ITER main parameters are reported in table1.1.

| Parameter | Value |
|---|---|
| Fusion power | 500 MW |
| Power gain factor Q | 10 |
| Pulse length | upto 3600s |
| Plasma major radius | 6.2m |
| Plasma minor radius | 2.0m |
| Plasma current | 15MA |
| Toroidal field at 6.2 m radius | 5.3T |

Table 1.1: ITER facility parameters [17]

To heat plasma up to 15keV (necessary operating temperature) two heating methods are implemented (see fig.1.5)[17]:

- RF waves: this method is based on creating RF wave and coupling them into the plasma (frequencies near to ion/electron cyclotron frequency 40-60 MHz and 170 GHz respectively).

- Neutral Beam Injector (NBI): the second method consists of producing deuterium/hydrogen ions, accelerating and neutralising them; then, accelerated particles can penetrate the plasma without being influenced by the magnetic field (see fig.1.6).

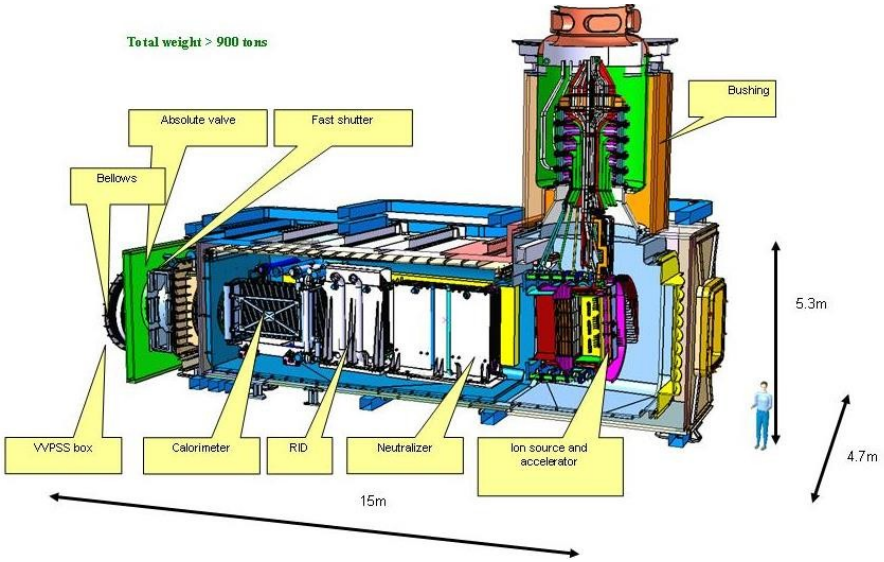


Figure 1.6: Neutral beam injector[17]

The ITER heating system consists of two NBI of 16.5MW each, that accelerate Hydrogen and Deuterium ions due to their high efficency in neutralisation efficiency. Due to the "stripping" (neutralisation of ions by backgrond gas before reaching full energy) process, extracted negative ion currents must be greater (of about 30%) than the required accelerated negative ion currents. The ratio between the co-extracted electron current and the negative ion current is required to be less than one. The Beam must have a divergence of less than 7mrad and an inhomogenity of extracted current of less than 10%[30]. Others parameters are reported in tab.1.2.

| **Parameter** | **ITER requirements** |
|---|---|
| Source dimensions | $1.9 \times 0.9 m^2$ |
| Source pressure | 0.3Pa |
| Extraction area | $0.2 m^2$ |
| Extracted current | 58 A for D− beam<br>68 A for H− beam |
| Accelerated current | 40 A for D− beam<br>49 A for H− beam |
| Electron content ($j_e$ /$j_{ion}$ ) | $\leq 1$ |
| Pulse length | 3600s |
| Uniformity | $\pm 10\%$ |
| Divergence | $\leq 7 mrad$ |

Table 1.2: ITER neutral beam system source requirements and parameters[30].

In Consorzio RFX is planned to build the ITER Neutral Beam Test Facility PRIMA[28][29] (**P**adova **R**eserch on **I**njector **M**egavolt **A**ccelerated), that is composed of two experimanetal devices called SPIDER (**S**ource for **P**roduction of Ion of **D**euterium **E**xtracted from **RF** plasma) and MITICA (**M**egavolt **ITER** **I**njector **C**oncept **A**dvancement): SPIDER is a full size Ion Source with low energy ion extraction (100keV)[8] and MITICA[28] is a full size neutral beam injector at full beam power. SPIDER aims at testing the extraction of negative ion beam made of $H^-$ and $D^-$ from a "real size" ITER ion source. Focus on SPIDER and its features: the main demands are to have an extracted $H^-/D^-$ current

density larger than 355/258 $A\ m^{-2}$, an energy of 100 keV and a pulse time duration of up to 3600s[8]. The extraction and accelerator system designed for SPIDER is composed of three grids (fig.1.7) called Plasma Grid (PG), Extraction Grid (EG), Grounded Grid (GG): on each grid there are 1280 apertures.

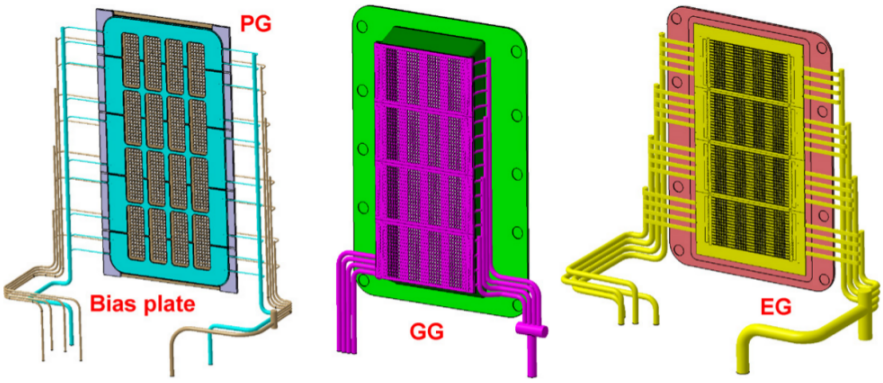


Figure 1.7: The tree grid system with their cooling circuits: plasma grid (PG), extraxtion grid (EG), grounded grid (GG)

On PG (kept at electric potential of -100kV with respect to the ground) ion particles are extracted from the ion source; ion production in the ion source occurs mainly through two types of processes[10][21]:

- volume process: is a dissociative attachment obtained after the excitation of high vibrational levels in the electronic ground state of the $H_2$ molecule (eq.1.7).
- surface process: it is based on the conversion of hydrogen particles impinging on the source walls (eq.1.8). This process is classified as atomic or ionic whether the Hydrogen particles are neutral or positive ions.

$$\begin{aligned} H_2 + e &\rightarrow H_2^*(v) + e \\ H_2^*(v) + e &\rightarrow H + H^- \end{aligned} \tag{1.7}$$

$$H, H^+ + e \rightarrow H^- \tag{1.8}$$

The efficiency of $H^-$ ion production is related to low work function of the material on the source wall: this characterstic is typical of the elements of the first group in the periodic table: in fact the choosen element for the layer on the wall surfaces is Caesium; moreover the PG is Molybdenum coated to decrease the sputtering yield and to extend the Caesium effect[8]. To lower electron density and temperature in order to increase the efficacy of the volume process a vertical current flows creating a so called "filter field". Between PG and EG (kept at electric potential of -90kV with respect to the ground) $H^-/D^-$ negative ions are properly extracted while the electrons collide on the grid. The GG accelerates ions up to 100kV and also compensates the beamlet deflections inside the accelerator. About beam optics the divergence is based on the divergence of $\frac{j_{ext}}{U^{3/2}}$: this relationship can be explained in relation of the Child-Langmuir law eq.1.9[12] that correlates extraction voltage $U$ to extraction current $j_{ext}$:

$$j_{ext} = \frac{4\epsilon_0}{9}\sqrt{\frac{2Ze}{m}}\frac{U^{3/2}}{d^2} \tag{1.9}$$

where $Z$ is the atomic number of extracted particles; $m$ the mass of extracted particles and $d$ the distance between grids. Ions, due to electric field, start to flow between PG and EG

and, at the same time, shield (in a distance comparable to Debye length 1.3) the electric field and it is to create a space charge density that fix the maximum current density.
An important parameter for the characterisation of beam optics is the perveance P, defined by eq.1.10:

$$P = \frac{I}{U^{3/2}} \tag{1.10}$$

The maximum value of perveance can be calculated through the use of eq.1.9:

$$P_0 = \frac{4\pi\epsilon_0}{9}\sqrt{\frac{2Ze}{m}}\frac{R^2}{d^2} \tag{1.11}$$

where $R$ is the radius of extraction apertures. Eq.1.11 is completely determined by the geometry of the grids and by the type of extracted particles.

## 1.4 Beam Diagnostics

A negative ion source facility, called ELISE, is being commissioned at IPP[5] and aims to an ITER-relevant extracted current density of negative ions[22] using a a large RF driven ion source with a pulsed extraction. Operational parameters are: plasma production up to 1 h, acceleration of negative ion beam up to 60kV for 1s every 180s via an ITER-like extraction system. To measure beam parameters there is a great variety of devices, depending on particle type, beam intensity, and particle energy[31]. ELISE is equipped with a simple beam dump, a sophisticated diagnostic calorimeter, a tungsten-wire calorimeter and Doppler shifted $H_\alpha$ beam emission spectroscopy (see fig.1.8)[22]:

- **Beam dump**: it consists of 4 HCP copper plates, 2cm thick, covering a total area of 1.2m×1.2m and is designed to stop an ion beam of 20A with up to 2° divergence. Beam dump is cooled down to room temperature during the pauses and water calorimetry allow a measure of total beam power. Moreover temperature is monitored by 4 thermocouples on the back side of each plate.

- **Diagnostic calorimeter**: it is a high resolution diagnostic calorimeter and is made of 4 HCP copper plates, each one approximately 600mm×600mm and equipped with 12 thermocouples to perform beam profile measurements.

- **Tungsten-wire calorimeter**: placed perpendicularly to the beam at 1.8m distance from acceleration grid; it consist of a grid of 100 tungsten wire (diameter 0.2m) spaced by 20mm each others and the two planes (wire are vertically and horizontally arranged) spaced 10mm. This diagnostic provides a qualitative image of beam position.1.8

- $H_\alpha$ **Doppler shift beam spectroscopy**: This diagnostic is perform to have a quantitative characterisation of the extracted beam in ELISE, the beam divergence and stripping losses.

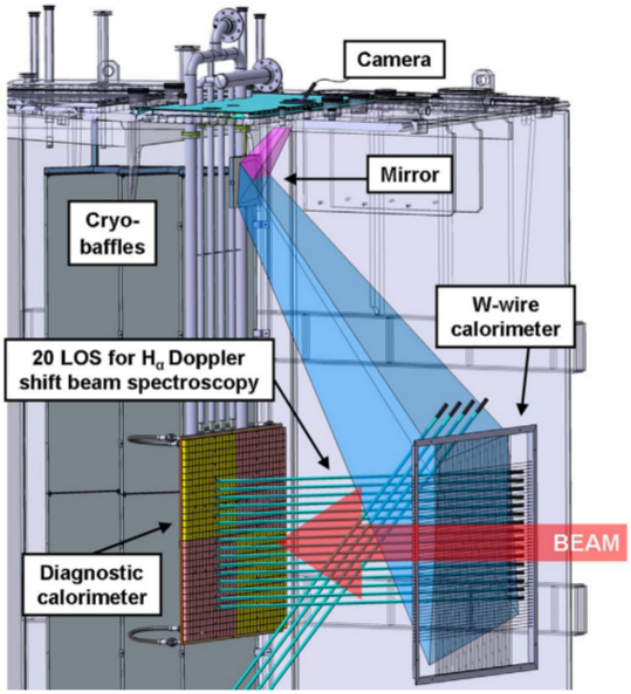


(a) *Beam diagnostic tools in ELISE.*

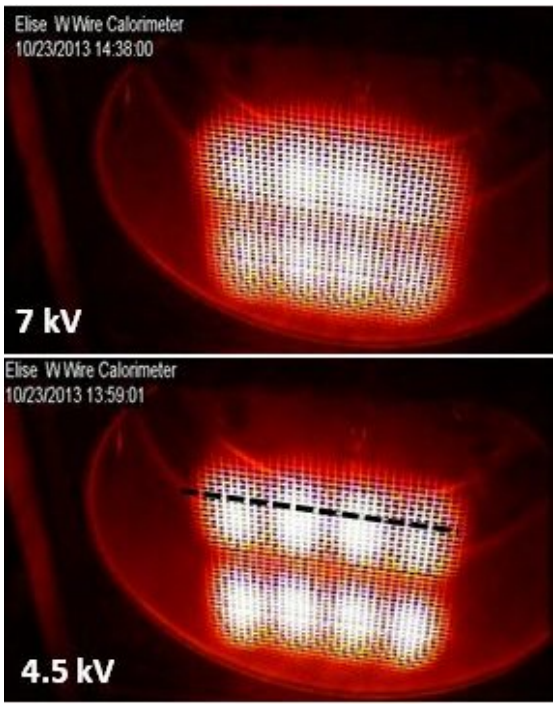


(b) *Image of W-wire calorimeter.*

Figure 1.8: Beam diagnostics of ELISE test facility[22] (left) and an image of W-wire calorimeter[16] (right)

## 1.5 Power balance in the wire

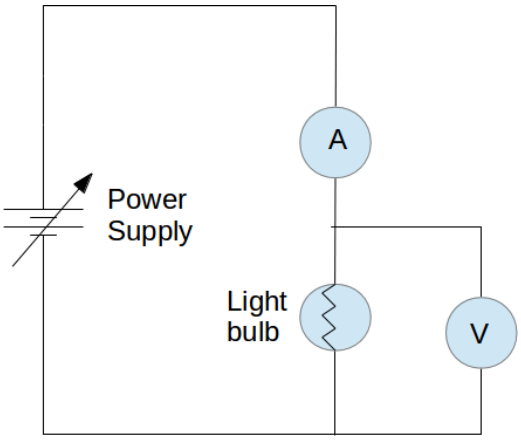


Figure 1.9: Electrical circuit

While the current flows, the wire is ohmically heated and (depending of wire length and radius) starts emitting light at a certain value of electrical power. The model that is taken in consideration is the grey body; consequently a value of different emissivity is used in the following formulas. The second effect that takes place along the wire is heat conduction. The equation [13] used is

$$VI = \sigma\epsilon(T^4 - T_e^4)S + kA\frac{T - T_c}{l^*} \qquad (1.12)$$

where $\sigma$ is the Stefan-Boltzmann constant, $\epsilon$ the emissivity, $k$ the thermal conductivity, $S$ the wire surface, $l^*$ the length along which the temperature gradient takes place, $A$ the wire section, $T$ the maximum wire temperature, $T_e$ the external temperature and $T_c$ the temperature at the ends of the wire to which conduction takes place. By replacing $S = 2\pi rL$ and $A = \pi r^2$ we find:

$$VI = \sigma\epsilon(T^4 - T_e^4)2\pi rL + k\pi r^2\frac{T - T_c}{l^*} \qquad (1.13)$$

The left-hand side of equation 1.13 is the power deposited via ohmic heating that must be equal to the right-hand side representing the power emitted through radiation and

conduction. In sections 1.5.1 and 1.5.2 I will explain the phenomena of heat conduction and greybody radiation. About the relationship between wire resistivity and temperature I consider two formulas:

$$\rho(T) = \rho_0 \left(\frac{T}{T_0}\right)^{1.2} \tag{1.14}$$

$$\rho(T) = \rho_0(1 + \alpha(T - T_0)) \tag{1.15}$$

where $\rho_0 = 5.25 \cdot 10^{-8}\Omega m$, $\alpha = 0.0053K^{-1}$, $T_0 = 293.15K$. Equation 1.14 [15] is valid in the range 1200°K - 3200°K while below 1200°K discrete resistance values are used [18]. Equation 1.15 is valid from 273°K to 3000°K [24] [7]. Equations 1.15, 1.14 and datas provided by Jones [18] have small differences in the range 300°K - 3200°K as seen in figures 1.10.

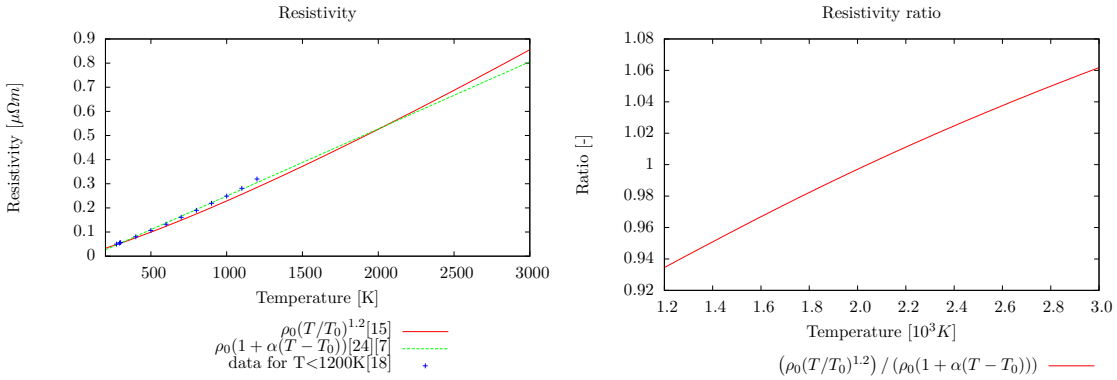


Figure 1.10: trend of resistivity as a function of temperature

I decide to use equation 1.15 and then I can calculate the wire resistance:

$$R(T) = \rho_0 \frac{L}{A}(1 + \alpha(T - T_0)) \tag{1.16}$$

where $L$ is the wire length, $A = \pi r^2$ the wire section. By replacing $V = R(T)I$ in 1.13 I obtain:

$$VI = R(T)I^2 = \sigma\epsilon(T^4 - T_e^4)2\pi rL + k\pi r^2 \frac{T - T_c}{l^*} \tag{1.17}$$

$$VI = \frac{V^2}{R(T)} = \sigma\epsilon(T^4 - T_e^4)2\pi rL + k\pi r^2 \frac{T - T_c}{l^*} \tag{1.18}$$

and using 1.16 in 1.18 and in 1.17 I finally find:

$$V^2 = \rho_0(1 + \alpha(T - T_0)) \left(\sigma\epsilon(T^4 - T_e^4)\frac{2L^2}{r} + kL\frac{(T - T_c)}{l^*}\right) \tag{1.19}$$

$$I^2 = \frac{\sigma\epsilon(T^4 - T_e^4)2\pi^2 r^3 + k\pi^2 \frac{r^4}{L}\left(\frac{T - T_c}{l^*}\right)}{\rho_0(1 + \alpha(T - T_0)} \tag{1.20}$$

### 1.5.1 Thermal Conductivity

Heat deposited along the wire concetrates in the middle creating a temperature gradient. The equation I consider says that heat flux is equal to:

$$\bar{q} = -\lambda\bar{\nabla}T \tag{1.21}$$

where $\bar{q}$ is the heat flux, $\lambda$ thermal conductivity and $\bar{\nabla}T$ the temperature gradient between two points. Considering the section fixed I can write:

$$q = \frac{H}{A} = -\lambda \frac{dT}{dl} \tag{1.22}$$

where $H$ is the conducted power[W] and $A = \pi r^2$ is the section crossed by the heat due to temperature gradient and, in case of a filament, depends on wire radius. Considering a steady-state case, the equation can be solved to get:

$$H = kA \frac{T - T_c}{l^*} \tag{1.23}$$

In the final equation written above $T$ and $T_c$ are condidered the filament temperature maximum and the temperature at the end of the wire respectively. $l^*$ is the length along which the temperature gradient take place; $l^*$ is different from the whole wire length and can be located only at the ends of the wire. Figure 1.11 is an example of incandescent wire observed by a CCD camera; the experimantal procedure will be explained in 2.3. In the figure it can be noticed the emission gradient along the wire and, consequently, the temperature gradient; during the experiment it was noticed that the copper blocks, as a first approximation, possess a uniform temperature.

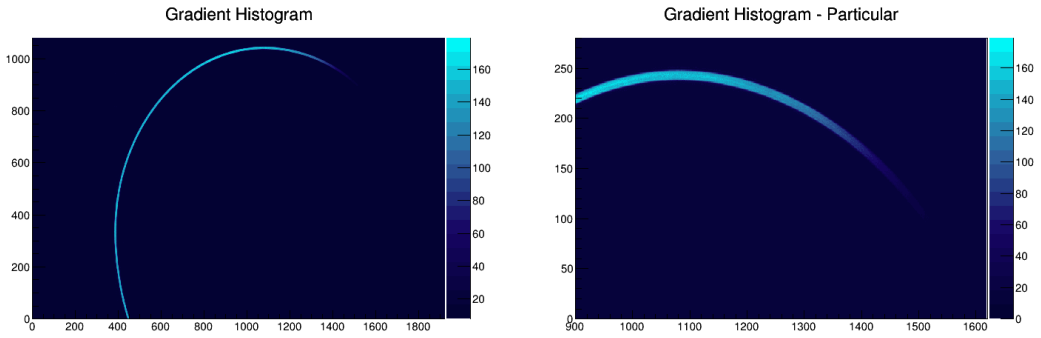


(a) *Wire Gradient.* (b) *Particular.*

Figure 1.11: Thermal conduction: wire gradient.

Published data of thermal conductivity show a dependence on temperature: ref. [11] reports:

$$\lambda(T) = \frac{1}{4.221 \cdot 10^{-3} + 5.436 \cdot 10^{-6} T - 1.595 \cdot 10^{-9} T^2 + 1.733 \cdot 10^{-13} T^5} \tag{1.24}$$

These data coincide with those reported in ref.[23] and in ref.[9]. The only reference that reports a significantly different dependence on $\lambda(T)$ is ref.[15] where the value of the thermal conductivity varies from 84 $WK^{-1}m^{-1}$ at 1000° K to 127 $WK^{-1}m^{-1}$ at 2800° K: probably an error occurred while tabulating data.

### 1.5.2 Grey Body Emissivity

In this first point of view the wire is considered as a grey body so the power emitted via radiation is:

$$\sigma \epsilon (T^4 - T_e^4) S \tag{1.25}$$

Where $T$ is the temperature of the wire, $T_e$ is the external temperature, $\epsilon$ is the emissivity, $\sigma = 5.67 \cdot 10^{-8} Js^{-1}m^{-2}K^{-4}$ is the Stefan-Boltzmann constant and $S$ is the total emitting

surface that, in our case, corresponds to the wire surface; so $S = 2\pi rL$ where $L$ is the wire length. Considering [14] the value of the emissivity changes depending on temperature from a value of 0.022 at 273°K to 0.334 at 3000°K; Ref. [24] reports a dependence of emissivity on the surface temperature T. Different relationship between emissivity and temperature might be ascribed to the surface conditions: oxidized filaments show a small dependence of emissivity on temperature, while bright metal surfaces show a substantial deviation from 1.13[13].
The problem of emissivity dependence on temperature is still unsolved. I decide to study the possible dependence of emissivity on temperature in the experiment phase after the baking process when the wire surface is bright and clean (see sec.2.3.2 and fig. 2.11).

# Chapter 2

# Preparation of the experiment

## 2.1 Requirements of the power supply

From equations 1.19 and 1.20 I have determined the requirements of power supply: its easy to see that every wire needs a different power to be heated up to a certain temperature and this means different current and voltage ranges. The thermal conduction term is negligible at high temperature as can be seen from the figure 2.1 and has anyway a minor effect.

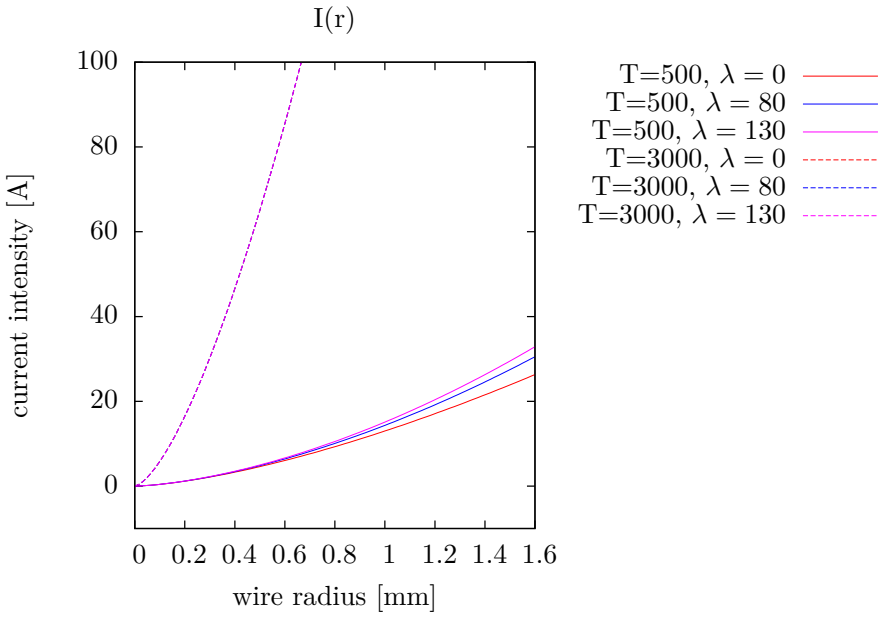


Figure 2.1: Parameters: $\epsilon = 0.3$, $L = l^* = 0.2m$

Figures 2.2 represent the trend of the current and the voltage as a function of temperature:

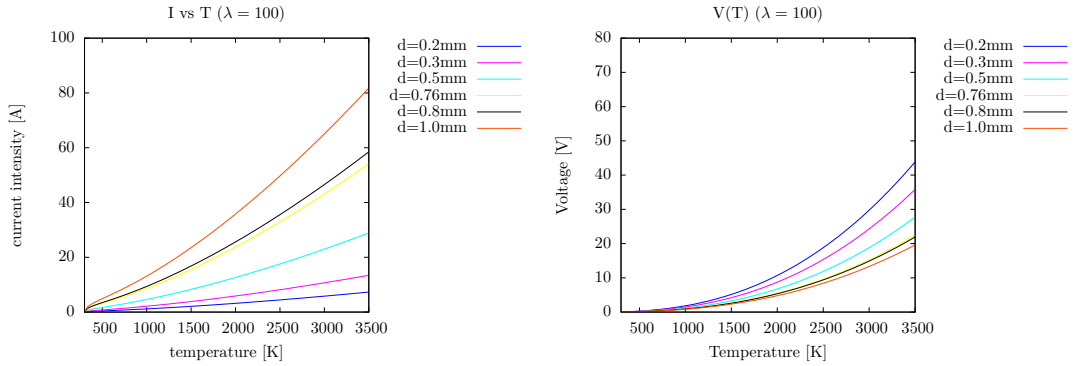


Figure 2.2: trend of the current and the voltage as a function of temperature using $\epsilon = 0.3$, $L = l^* = 0.2m$

Using figure 2.2 I define the power supply electrical characteristics: for the thicker wire to reach a temperature of about 3500°K is necessary a current of about 80A with a voltage of about 20V; for the thinner wire is necessary a current of 7A with a voltage of 44V.

## 2.2 Preparation of tungsten wires

The first tested wire is built with thoriated tungsten (fig. 2.3 lefthand) and has a radius of 0.38 mm, other wires (fig. 2.3 righthand) were prerared made of tungsten with different diameters: 0.2mm, 0.3mm, 0.5mm, 0.8mm, 1.0mm, 1.5mm (1.5mm not studied). Wires are connected to the vacuum feedthrough by copper blocks. The complete design is described in ref. [32].

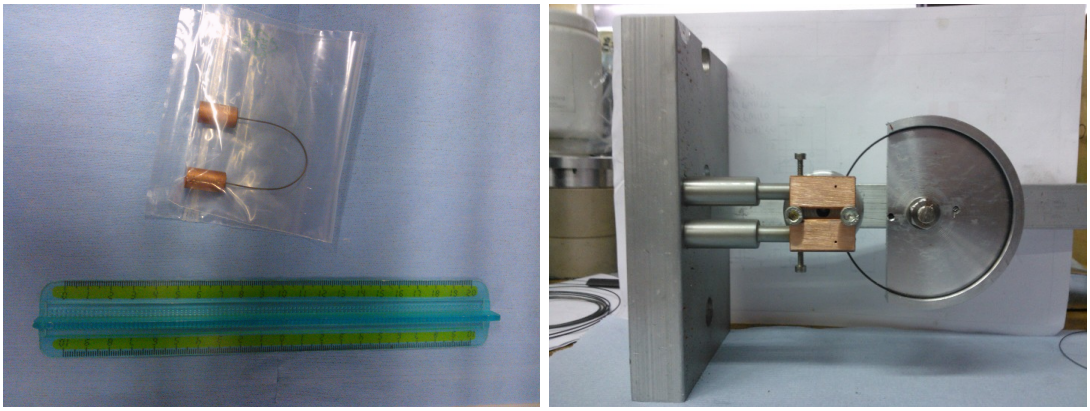

Figure 2.3: Wire made of thoriated tungsten (left); tools to weld the tungsten wire to the copper blocks (right)

## 2.3 Experimental setup

The main purpose is to heat the wire and to collect data with a CCD Camera (ref.[19]) positioned outside the vacuum chamber at a sufficient distance to both have a good number of pixel inside the wire while retaining the possibility to focus on the wire. The apparatus is composed of a vacuum chamber connected with a vacuum pump. The plane on which the wire is lying is almost perpendicular to the CCD camera. At first the wire plane was

horizontal but, due to gravity (particularly for the thinner wires) wire is bent and goes out of focus. The final arrangement is with the wire plane vertical and the CCD camera line of sight horizontal, in the same side as the CCD camera a spectrograph[6] is fixed: see figures 2.4 and 2.5.

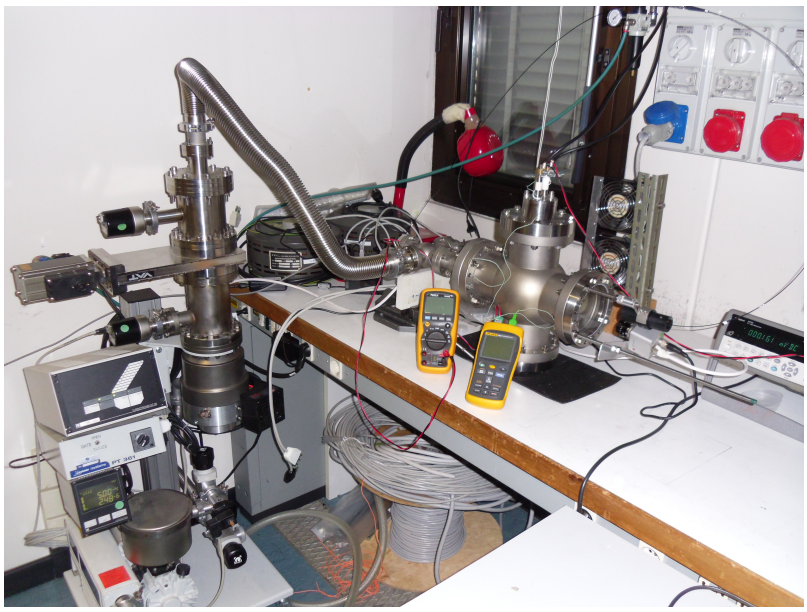

Figure 2.4: Experimental device

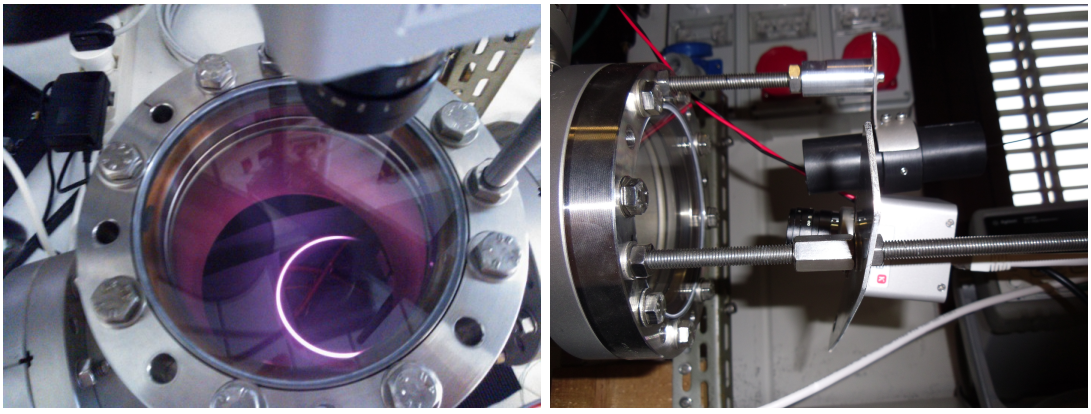

Figure 2.5: Experimental device: particular of hot wire and camera (left); camera and spectrograph (right)

Termocouples are used to read internal (one termocouple is fixed to a copper block) and external temperatures; two voltmeters are used to read internal (signal check at copper junctures) and external voltages and a current clamp measures the current. A power supply (EUTRON BVR2000 40V 45A) provides current for the tungsten wire. At first the CCD camera is fixed in a position and, before measuring, is focused on the wire; it has an adjustable shutter, which was always as closed as possible. Also the spectrograph is focused on the wire and measures light emitted in a range from 300nm to 850nm in order to have an independent measure of T. Spectra were acquired only for few wires: at first the instrument saturated due to strong brightness so it was decided to place, in front of the

spectrograph, a filter with value 3 (meaning a factor of $10^3$ of attenuation of the incoming light); the spectrograph is then calibrated and ready to acquire spectra that are analysed separately (ref. [32]) and only results are given here. Light spectra with the CCD camera are acquired with different integration times taking particular care that the signal does not saturate. A complete list of used quantities measured is reported below:

- temperature of the copper blocks (thermocouple "Type K")
- temperature of the feedthrough electrodes (thermocouple "Type N")
- current as indicated by the power supply display
- current as indicated by the current clamp (LEM LH2015)
- voltage drop between the feedthrough electrodes (Multimeter AGILENT 34410A)
- voltage drop between copper blocks (NIMEX NI 4600)
- pressure (Leybold PTR90 and Leybold TERMOVAK TTR 91)

### 2.3.1 The CCD Camera

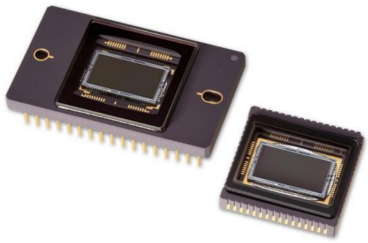

Figure 2.6: CCD sensor [19]

Using the camera programme[27] to acquire images I can regulate the integration time [ms/$\mu$s] up to a minimum of 1$\mu$s and the gain [dB] in a range from 0dB to 18dB: both these operations are linear. Collected images have an offset: the black part of the images has a mean value different from zero. and is subject to fluctuations due to background light radiation, the mean value of the background and the amplitude of fluctuations are independent from the integration time but not on the gain: the mean value is the same but fluctuations are larger (see fig.2.7 and fig.2.8).

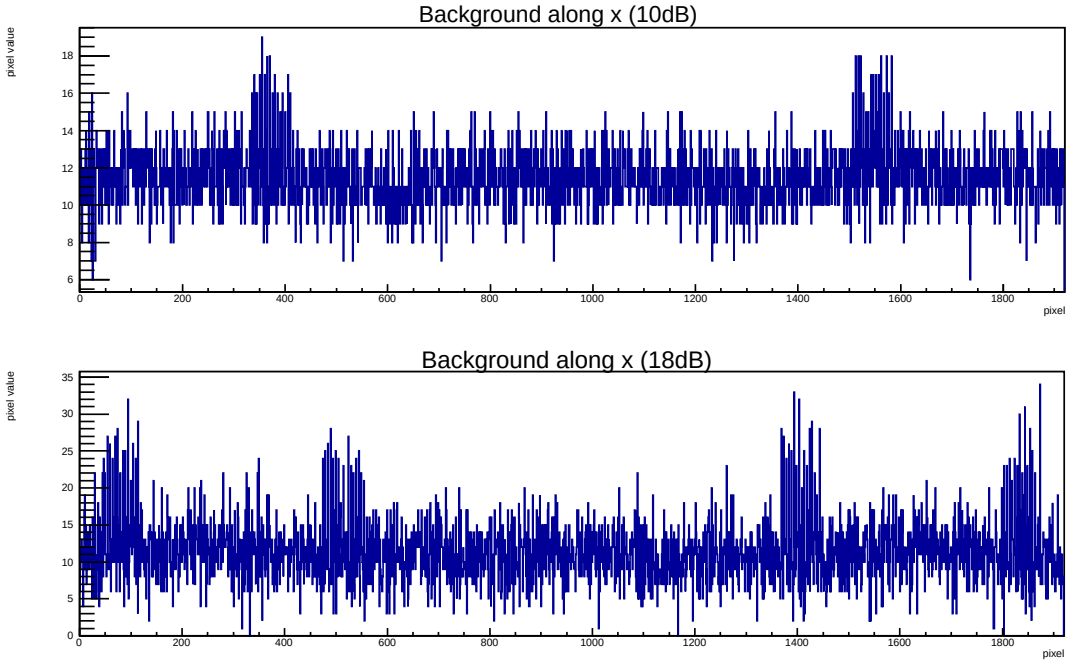


Figure 2.7: Background fluctuation in case of different gain (Data set 21/07 1mm)

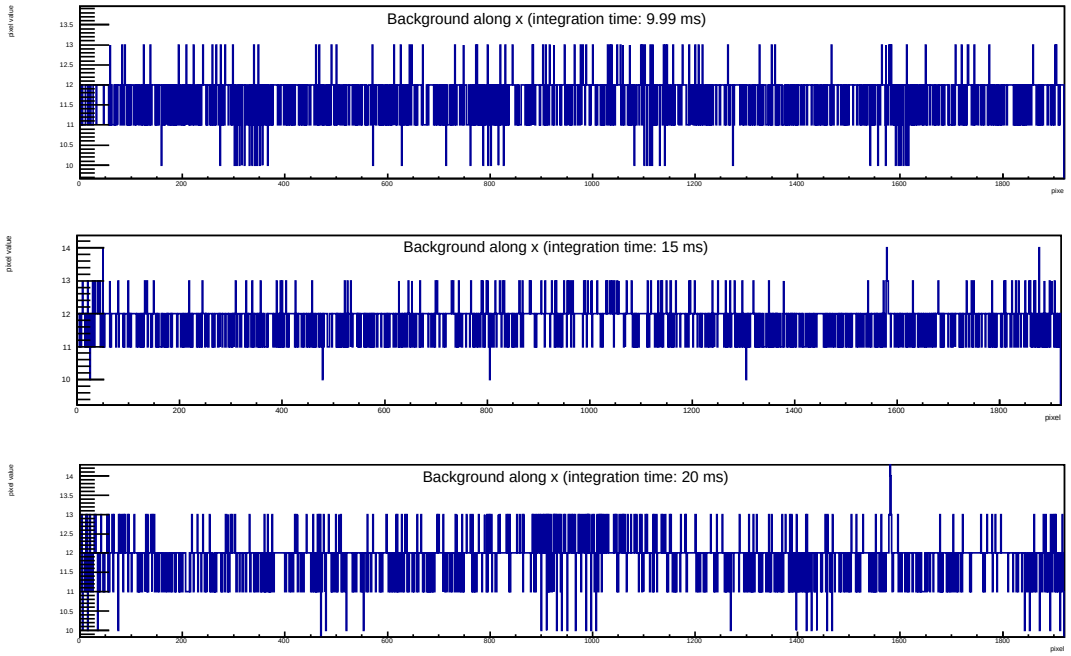


Figure 2.8: Background fluctuation in case of different integration times (Data set 18/07 1mm)

### Linearity of gain and integration time

I checked the linearity of the gain acquiring different images at fixed integration time. Data acquired refer to 21/07 with a wire diameter 1.0mm and to 29/08 with a wire diameter 0.3mm. In figure 2.9 data with linear fit: result of the fit are reported in tab. 2.1.

| Coefficients | Data Fit 21/07 | | Data Fit 29/08 | |
|---|---|---|---|---|
| | value | error | value | error |
| slope | 0.092 | ±0.008(9%) | 0.0045 | ±0.0005(10%) |
| intercept | -0.5 | ±0.1(23%) | -0.024 | ±0.007(28%) |

Table 2.1: Gain linearity: fit result

In a similar way I checked the linearity of the integration time: I acquire different images at a fixed gain. Data acquired refers to 16/07 with a wire of 0.8mm. In figure 2.9 data with linear fit: result of the fit are reported in tab.2.2.

| Coefficients | Data Fit 16/07 | |
|---|---|---|
| | value | error |
| slope | 3.32 | ±0.03(1.2%) |
| intercept | -5.1 | ±1.9(39%) |

Table 2.2: Linearity of the integration time: fit result

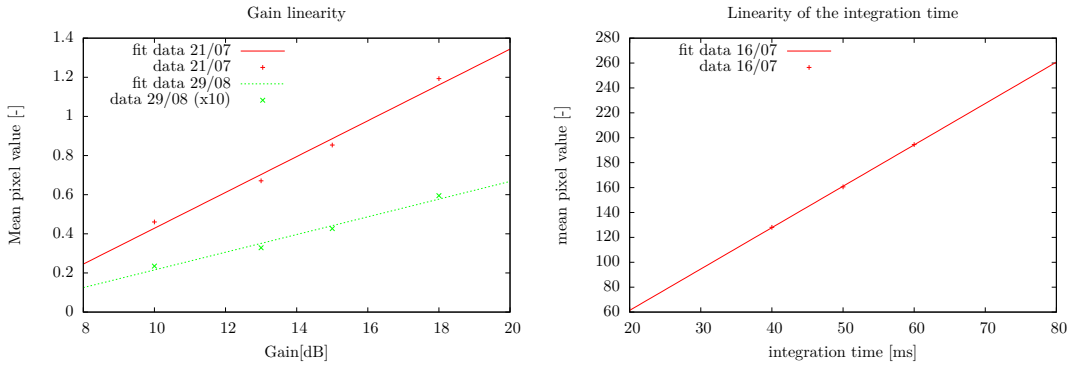


Figure 2.9: Gain linearity (left) and integration time linearity (right): fit

### Unwanted effects

The CCD camera is affected by two different phenomena which I call ”points of light” and ”light stripes”. ”Points of light” occurs at high integration time (above 300ms) and is amplified by the gain: it consists of a series of white pixel randomly arranged that increas the value of the background. These pictures are regularly excluded from the analysis . The second effect, called ”light stripes” occurs al low integration time: luckily the effect does not occur in the interesting area (the central part of the wire) and is easily eliminated by calculating the background and subtracting it from the signal. Figure 2.10 histograms represent the pixel value along a line not crossing the wire.

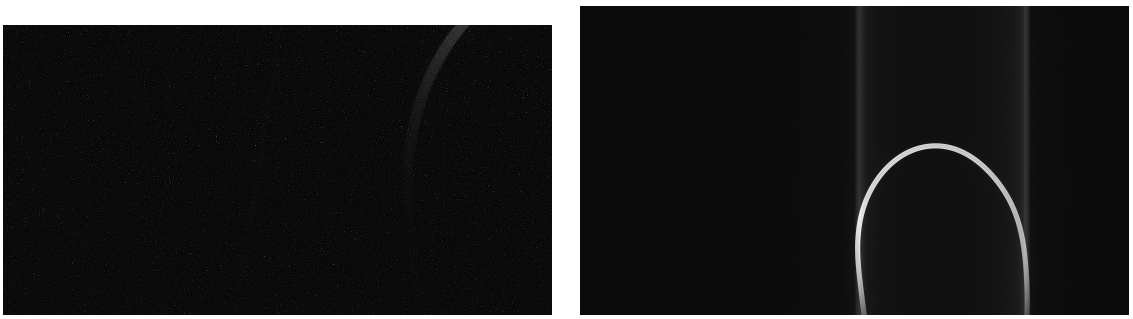

(a) *Points of light.*

(b) *Light Stripes.*

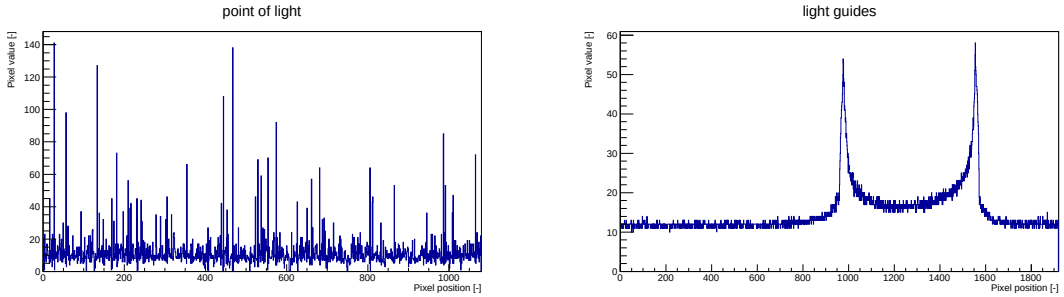


(c) *Points of light: analysis.*

(d) *Light stripes: analysis.*

Figure 2.10: CCD camera phenomena

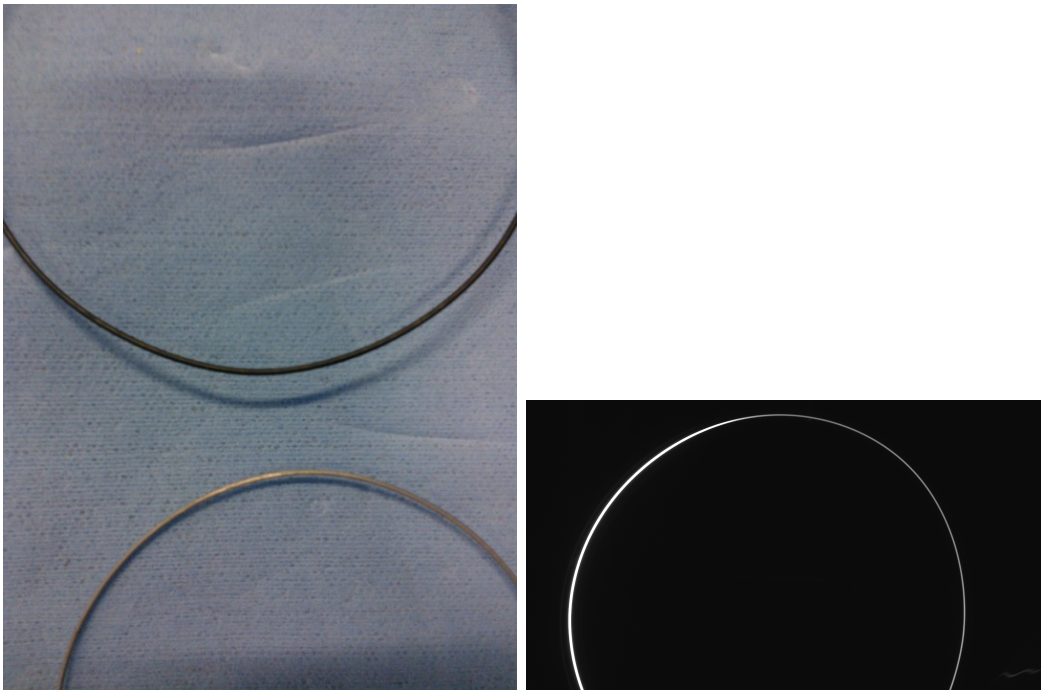

Figure 2.11: Surface aspect after (down) and before (up) heating (left) and an image of the wire, while baking, taken with the CCD camera

### 2.3.2 Experimental procedure

Until the temperature reaches about 3000° K, the current increment is 0.5A and, step by step, data are collected only when voltage stabilizes: this can take tens of seconds especially in the early measures [7]. Step by step about three images are collected with the CCD camera with different integration time. When signal is visible in the spectrograph also spectra are collected. Before breaking the tungsten wire, current was decresed of fixed current step and once again increased (always by steps) to about 3000°K: step by step electrical measures are taken. Until the wire breaks, at about 3600°K, the current step is 0.3A or 0.2A. Only wires with diameter 0.2mm, 0.3mm and 0.5mm are broken while thicker wires are only heated. The first analysed wire was the thoriated one and it doesn't present a characteristic observed instead with all others wire; the second type of wires, made of pure tungsten, present a particular effect at about 1300°K: suddenly there is an abrupt increase of voltage and strong increase of light emission. This effect may be caused by a baking process that occurs at a specific temperature and expels impurities from tungsten: impurieties are added to Tungsten during the wiredrawing to give flexibility to the material. This effect takes place for every tungsten wire at about the same temperature; the final result is a wire that is grayish white, lustrous and so fragile that thicker wires break while disassebling (see fig.2.11).

# Chapter 3

# Data Analysis

## 3.1 BigAnalisi.C

The main purpose is to measure the light emitted by the hotter part of the wire, in this case the central one. Several images with different integration time are collected to prevent the lack of information in case of saturation, always possible during data collection: these cases are always recognizable when compared to others images at the same current because the total sum of pixel value in a certain area is significantly lower. Images with gain different to zero, about three or four for each data set, are discarded from the analysis because not relevant and because they are affected by the "points of light" effect. The result of the analysis is a number that represents the light emitted in a certain area of the wire at a given temperature calculated by inverting the relationship 1.15 where $R(T) = \frac{V}{I}$ and $V$ and $I$ are obtained from the power supply and from the internal voltmeter measure respectively.
Each figure has been analysed by a macro written in ROOT called "BigAnalisi.C" that uses the "TASImage" class that provides the possibility to create, from each figure, a one-dimensional array containing pixel values. In order to trasform the array in a more user-friendly and suitable form the program uses a defined function called Index() that introduces xy-coordinates and allows easy changes in case of different position of the camera with respect to the Tungsten wire as seen in figures 3.1.
The user defines, for each data set, two horizontal and vertical stripes respectively, where

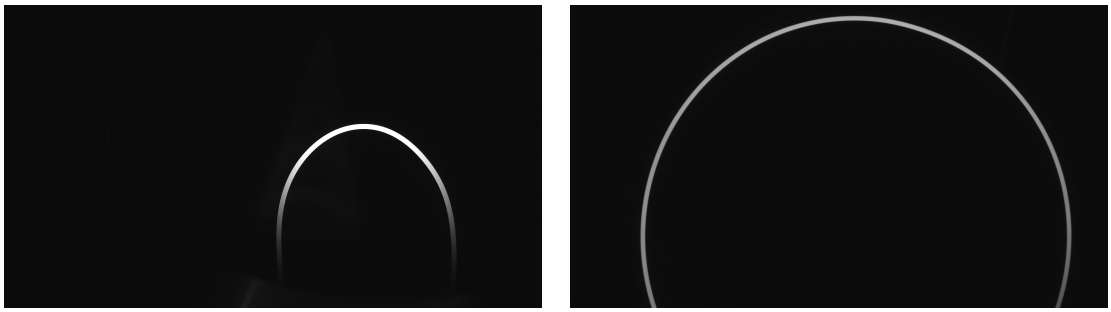

(a) *Wire position 1.* (b) *Wire position 2.*

Figure 3.1: Different wire positions

the program, for each figure, calculates in the first case the background and in the second case the pixel mean value.

### 3.1.1 Background fluctuations

In this specific device the background fluctuations is a random signal with a constant power spectral density so the mean values is computed from a pixel window as wide as possible in a black area of the figure. Unluckily the presence of the "light guides" effect, that has't a constant mean value, forced to find a new way to subtract the background. By knowing that along vertical lines the background has a costant profile I decide to subtract, line by line, the pixel mean value of a part of the line where the signal is not present. In fig. 3.2 I reported an example of the subtracted background: in every bin I plot the value of background calculated as a mean of 22 pixels in each line.

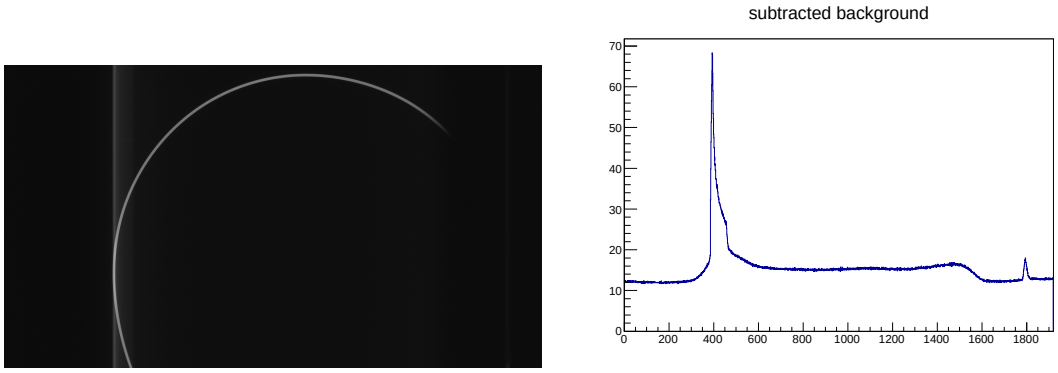


(a) *Image.* (b) *Background.*

Figure 3.2: subtracted background

### 3.1.2 The Signal

The user defines for each figure a "x" or "y" window with respect to wire orientation (e.g. if the meaningful part of the wire is parallel to the "x" axis then the range is along the "x" axis centered in the hotter part of the wire and wide about 100 pixels and as long as the image length). This choice must be repeated for every data set because the experimental device has no fixed reference with respect to the wire and the camera must be adjusted every time before data collections. Moreover, while heating, the wire changes its profile (it expands due to the tension of the wire or it tilts due to gravity). In the selected range every row or column (as the case "x-range" or "y-range") is read as histogram; then the background signal is subtracted from each bin and finally all bins are divided by the itegration time (different in each figure). Lastly the programm finds, for every line, the maximum bin value and sums together all the pixels that are at least 3/4 of the maximum value so the total sum increases while reading lines. Meanwhile the program counts how many pixels were added and finally divides the total sum by total counts obtaining the mean value of the signal in the selected window. The result is obviously a relative measure of the light emitted by the wire while heating.

## 3.2 Fit of power vs temperature

I developed this program to determine, by an interpolation, the value of the emissivity $\epsilon(T)$ and the value of thermal conductivity $\lambda$ using the measured values of voltage and current and the temperature obtained by eq.1.16. At first was considered eq.1.19 to build a fit with voltage data: the first problem I encountered was the presence of a square root

that gives convergence problems; so I decided to make the fit of the squared data voltages, however, in this way, only half of the available data was used: in fact I would not use the current data apart from the estimation of temperature; moreover the equation I should have used (eq. 1.18) has not a linear form (it is composed of two parts multiplied together). At the end the relationship I consider is eq.1.13; I suppose, for the emissivity, a power law dependence on temperature based on literature as discussed in sec.1.5.1:

$$\epsilon(T) = \mathbf{p0}T^{\mathbf{p1}} \tag{3.1}$$

As for thermal conductivity $\lambda$ and thermal gradient length $l^*$ a single parameter is used:

$$\mathbf{p2} = \frac{\lambda}{l*} \tag{3.2}$$

So the final function fitted to the experimental data is:

$$VI = \mathbf{p0}T^{\mathbf{p1}}\sigma 2\pi rl(T^4 - T_0^4) + \mathbf{p2}\pi r^2(T - T_c) \tag{3.3}$$

I decide to fix the value of $T_0$ and $T_c$ at 350°K and 300°K respectively. Sometimes the fit result gave a negative value of parameter $p2$ so I forced it to be positive by replacing $p2$ with $\sqrt{\mathbf{p2}^2}$:it means that the **p2** can be computed as negative but it is used as a positive quantity in the final equation. First results show that the value of **p2** changes depending on the radius and on the starting value in the fit program: the fit was compared with different starting values of the parameter **p2** and with the fixed value of **p2** equal to 0; I got the results reported in table 3.2. It is found that both fits with fixed and variable parameters are good with respect to the data but parameters **p0** and **p1** give incoherent results (see tab.3.2). Using the considerations in 1.5.1 and considering the fact that a good fit is obtained when imposing value of **p2** and in case of free **p2** parameter I decide to fix **p2** parameter equal to 0. In fig.3.3 I report the same data fitted using the two methods illustrated above: **p3**, **p4**, **p5** represent $T_0$,$T_c$ and the radius $r$ respectively.

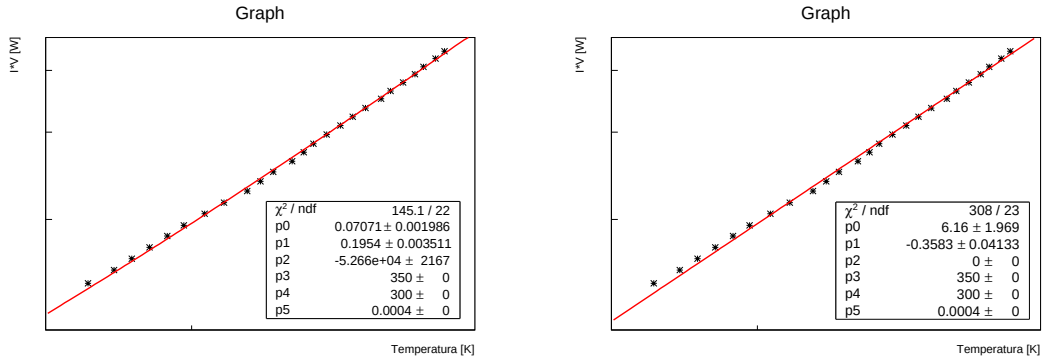


(a) *Fit with **p2** free parameter (data 18/07 0.8mm).* (b) *Fit with **p2** fixed to 0 (data 18/07 0.5mm).*

Figure 3.3: Data 24/07, diameter=0.5mm, two fitting methods

The final method adopted in data analysis fixes the **p2** parameter to 0 and treats the emissivity as a constant: so **p1** equal to 0 and **p0** a free parameter. Results in this case are reported in tab3.3; Some fits do not converge or give wrong results as shown in fig.3.4, these results are not reported. In fig.3.4 examples of fit are reported.

| **p2** start. value | | 0(fixed) | 0 | 10 | 100 | 1000 |
|---|---|---|---|---|---|---|
| | p2 | 0 | 1.20E+004 | 4.42E+004 | 4.44E-004 | 5.86E+004 |
| set1 | p1 | 0.028 | 0.178 | 0.6592 | 0.6571 | 0.9129 |
| | p0 | 0.373 | 0.1138 | 0.002558 | 0.002595 | 0.000347 |
| 16/06 0.8mm | p2 | 0 | 2.24E+004 | 3.22E+004 | 3.22E+004 | 3.23E+004 |
| set2 | p1 | -0.05 | 0.51 | 0.9002 | 0.9002 | 0.9003 |
| | p0 | 1.8 | 0.03127 | 0.001853 | 0.001853 | 0.001852 |
| **p2** start. value | | 0(fixed) | 0 | 10 | 100 | 1000 |
| | p2 | 0 | 4770 | 2.49E+004 | 2.49E+004 | 2.49E+004 |
| set1 | pi1 | 0.02 | 0.11 | 0.7313 0.7313 | 0.7313 | |
| | p0 | 1.15 | 0.597 | 0.006524 | 0.006524 | 0.006524 |
| 18/07 0.8mm | p2 | 0 | 5.27E+004 | 1.05E+005 | 1.05E+005 | 1.05E+005 |
| set2 | pi1 | -0.4 | 0.1954 | 1.089 | 1.089 | 1.089 |
| | p0 | 6.16 | 0.07071 | 5.60E-003 | 5.60E-003 | 5.60E-003 |
| **p2** start. value | | 0(fixed) | 0 | 10 | 100 | 1000 |
| | p2 | | 1.80E+004 | 1.80E+004 | 1.80E+004 | 1.80E+004 |
| set1 | p1 | | 0.5619 | 0.5619 | 0.5619 | 0.5619 |
| | p0 | | 0.01725 | 0.01725 | 0.01725 | 0.01725 |
| 18/07 1.0mm | p2 | | 6.35E+004 | 9.54E+004 | 9.54E+004 | 0.0001479 |
| set2 | p1 | -0.91 | 0.1259 | 1.241 | 1.241 | 0.9175 |
| | p0 | 361.8 | 0.08142 | 1.13E-005 | 1.13E-005 | 8.81E+004 |
| **p2** start. value | | 0(fixed) | 0 | 10 | 100 | 1000 |
| | p2 | 0 | 3493 | 8696 | 9159 | * |
| set1 | p1 | -0.29 | -0.1665 | -0.03414 | -0.01423 | * |
| | p0 | 2.78 | 1.113 | 0.3913 | 0.003347 | * |
| 21/07 1.0mm | p2 | 0 | 8256 | * | * | * |
| set2 | p1 | -0.29 | -0.084 | * | * | * |
| | p0 | 2.783 | 0.561 | * | * | * |
| **p2** start. value | | 0(fixed) | 0 | 10 | 100 | 1000 |
| | p2 | 0 | 1.11E+004 | 4075 | 5480 | 4976 |
| set2 | p1 | 0.015 | 0.1576 | 0.07456 | 0.091 | 0.088 |
| | p0 | 0.2784 | 0.09 | 0.1746 | 0.1538 | 0.157 |
| 22/07 0.5mm | p2 | 0 | * | * | * | * |
| set2 | p1 | -0.32 | * | * | * | * |
| | p0 | 3.81 | * | * | * | * |
| **p2** start. value | | 0(fixed) | 0 | 10 | 100 | 1000 |
| | p2 | 0 | 1.20E+004 | 7261 | 5306 | 6955 |
| set1 | p1 | -0.07 | 0.1661 | 0.06678 | 0.0386 | 0.06297 |
| | p0 | 0.403 | 0.06324 | 0.138 | 0.1725 | 0.1422 |
| 24/07 0.5mm | p2 | 0 | 6.10E+004 | 6.01E+004 | 1.39E+005 | 1.34E+005 |
| set2 | p1 | -0.38 | -0.13 | -0.1432 | 0.2117 | 0.196 |
| | p0 | 4.542 | 0.5956 | 0.6296 | 0.0316 | 0.03625 |
| **p2** start. value | | 0(fixed) | 0 | 10 | 100 | 1000 |
| | p2 | 0 | 5899 | 7057 | 0.0039 | 0.000565 |
| set1 | pi1 | -0.03 | 0.0264 | 0.03654 | -0.0251 | -0.02513 |
| | p0 | 0.251 | 0.1654 | 0.1525 | 0.2507 | 0.2507 |
| | p2 | 0 | * | * | * | * |
| set2 | pi1 | -0.13 | * | * | * | * |
| | p0 | 0.597 | * | * | * | * |
| 29/08 0.3mm | p2 | 0 | 4105 | 14.54 | 635.8 | 3227 |
| set3 | p1 | 0.098 | 0.1275 | 0.1122 | 0.1148 | 0.1379 |
| | p0 | 0.101 | 0.07974 | 0.09048 | 0.08858 | 0.07353 |
| | p2 | 0 | * | * | * | * |
| set4 | p1 | 0.043 | * | * | * | * |
| | p0 | 0.142 | * | * | * | * |
| **p2** start. value | | 0(fixed) | 0 | 10 | 100 | 1000 |
| | p2 | 0 | 3.61E+004 | 5.17E+004 | 3.76E+004 | 4.96E+004 |
| set1 | pi1 | -0.39 | -0.2854 | -0.2015 | -0.2263 | -0.2292 |
| | p0 | 5.194 | 2.194 | 1.11 | 1.367 | 1.386 |
| 04/09 0.2mm | | | | | | |

Table 3.2: fit result; *:fit doesn't converge

| **p0** | set | value | error |
|---|---|---|---|
| 16/07 0.8mm* | set2 | 0.462 | 0.002 |
| 18/07 1.0mm* | set2 | 0.322 | 0.004 |
| 21/07 1.0mm* | set1 | 0.318 | 0.001 |
| | set2 | 0.311 | 0.002 |
| 22/07 0.5mm | set1 | 0.302 | 0.002 |
| | set2 | 0.314 | 0.001 |
| 24/07 0.5mm | set1 | 0.237 | 0.001 |
| | set2 | 0.210 | 0.001 |
| 29/08 0.3mm | set1 | 0.206 | 0.001 |
| | set2 | 0.202 | 0.001 |
| | set3 | 0.219 | 0.001 |
| | set4 | 0.209 | 0.001 |
| 04/09 0.2mm | set1 | 0.231 | 0.003 |

Table 3.3: final it result; *good only for high temperature (T>1000°K)

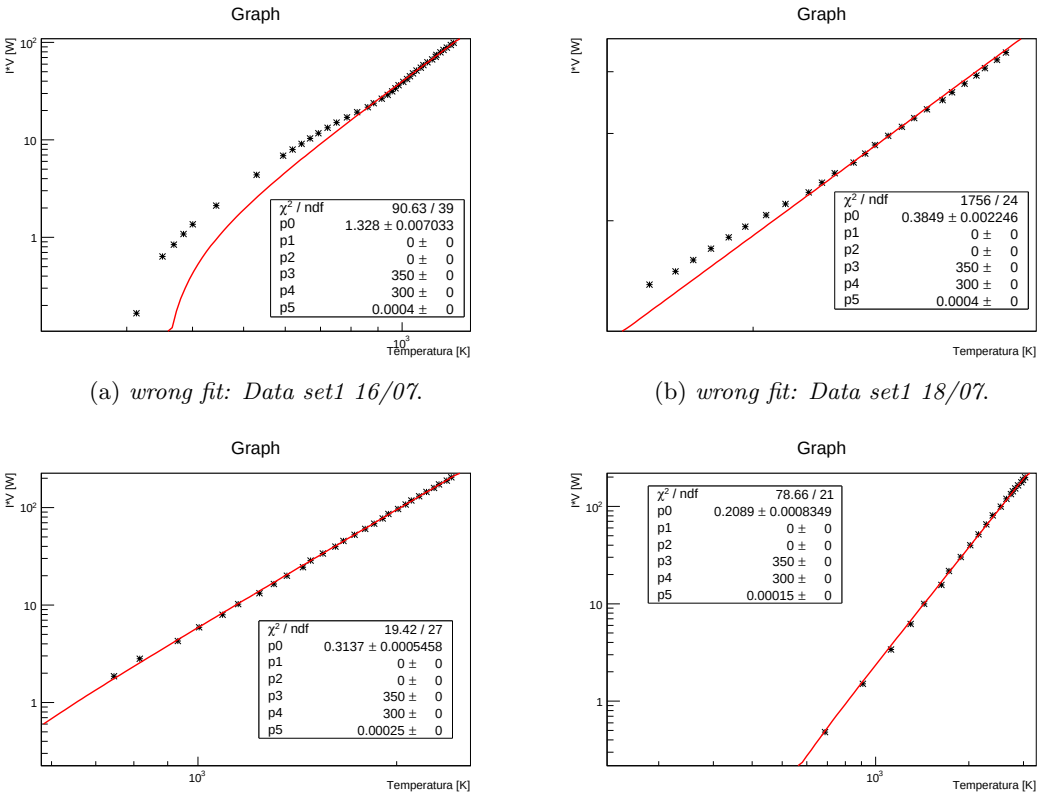


(a) *wrong fit: Data set1 16/07.*

(b) *wrong fit: Data set1 18/07.*

(c) *good fit: Data set2 22/07.*

(d) *good fit: Data set4 29/08.*

Figure 3.4: Fit results

The conclusion of these analyses shows that thermal conduction (eq.1.23) influences data only at low temperature and that the conductive term is relevant only in case the section of the wires is large enough. Emissivity is estimated as a constant, and excluding data that properly fitted only at high temperature an average value obtained from the analyses is:

$$\epsilon = 0.25 \tag{3.4}$$

Information obtained by fitting emitted light as a function electrical power (ref.[32]) shows

that the length of the wire is increased by about 20% during the experiment: this discrepancy (the wire length was verified by direct measurement) may be due to a variation of the radius of the wire. As a whole the product $\epsilon rl$ can be assured to be affected by an error of approximately 20%.

# Chapter 4

# Wire calorimeter simulations

A simulation is performed to obtain predictions about the behaviour of a wire hit by a two dimensional arrangement of beamlets: in particular, the time at which they reach the equilibrium depends on the wire radius; the temperature profile along vertical and horizontal wires depends on wire radius, beamlet divergence and energy flux as well as on the alignment of the wire with the column or row of beamlets. Aim of the simulations is the definition of a suitable arrangenment of wires as well as their diameters in order to characterise SPIDER beam. Simulations will be supplemented by considerations related to the effect of sputtering and to reasonable visible cameras Results give fundamental information on maximum temperature along wire, on temperature gradient between temperature peaks, on emitted radiation (using eq.1.25).

## 4.1 Numerical model

The simulations are performed in the COMSOL Multiphysics environment which is a simulation software based on the finite element technique. The finite element method is a numerical technique used to find approximated solutions to boundary value problems for partial differential equations. There are several possible choices about the model that describes the wire hit by the beamlets: simulation can be three-, two- or one-dimensional and can be solved in steady-state conditions or as a transient. I decided to build a one-dimensional model because the wire diameter is much thinner than the beam profile and the expected characteristic time for temperature stabilisation is much shorter than the propagation time along the wire radius; moreover a 1D model requires a much shorter solution time. As the model used is one-dimensional, the wire is represented as a segment, and the equation, that COMSOL solves, combines heat transfer equation, the presence of a heat source and the emitted radiation (see eq. 4.1):

$$\delta_{ts}\rho C_p \frac{\partial T}{\partial t} - \nabla(k\nabla T) = Q + C_{trans}(T^4_{ambtrans} - T^4) \tag{4.1}$$

where $C_{trans}(T^4_{ambtrans} - T^4)$ represents the emitted radiation power per unit volume, $T_{ambtrans}$ is room temperature; $Q$ is the power per unit volume deposited by the incident beamlets; $\nabla(k\nabla T)$ is power per unit volume conducted along the wire and $k$ the thermal conductivity; $\rho$ the Tungsten density and $C_p$ the specific heat.
The modelization is based on the conservation of the heat sources so parameters of eq.4.1 must be supplied: the power collected by a wire subjected to an energy flux $F$ must be input to the simulation as a generation of energy per unit volume; so the energy flux is integrated over the wire surface exposed to the beam ($2rl$) and divided by the volume

$(\pi r^2 l)$ to obtain:

$$Q = F\frac{2rl}{\pi r^2 l} = \frac{2F}{\pi r} \tag{4.2}$$

in the same way I compute the value of $C_{trans}$; in this case the whole wire surface emits:

$$C_{trans}(T^4_{ambtrans} - T^4) = \epsilon\sigma\frac{2\pi rl}{\pi r^2 l}(T^4_{ambtrans} - T^4) = \frac{2\sigma}{r}(T^4_{ambtrans} - T^4) \tag{4.3}$$

$$C_{trans} = \epsilon\frac{2\sigma}{r} \tag{4.4}$$

from considerations in sec.1.5.1 and sec.3.2, the relationships of thermal conductivity $\lambda$(eq.1.24) and emissivity $\epsilon$ (eq.3.4) as functions of temperature are deduced, respectively. Another needed parameter is the specific heat $C_p$ dependence on temperature: the relationship used is eq.4.5[11] which is in agreement with ref.[23] and ref.[9].

$$C_p(T) = 0.131 + 1.73\cdot 10^{-5}T \tag{4.5}$$

The total power deposited by the SPIDER beam of full performances is $4\cdot 10^6$ W distributed among 1280 beamlets arrenged in 16 groups (four columns composed of four beamlets groups, each spaced 80mm in horizontal and 60mm in vertical). Every beamlet group is composed of 80 beamlets arranged in five columns of 16 beamlets each (beamlets spaced 20mm horizontally, 22mm vertically) (see fig.4.1).

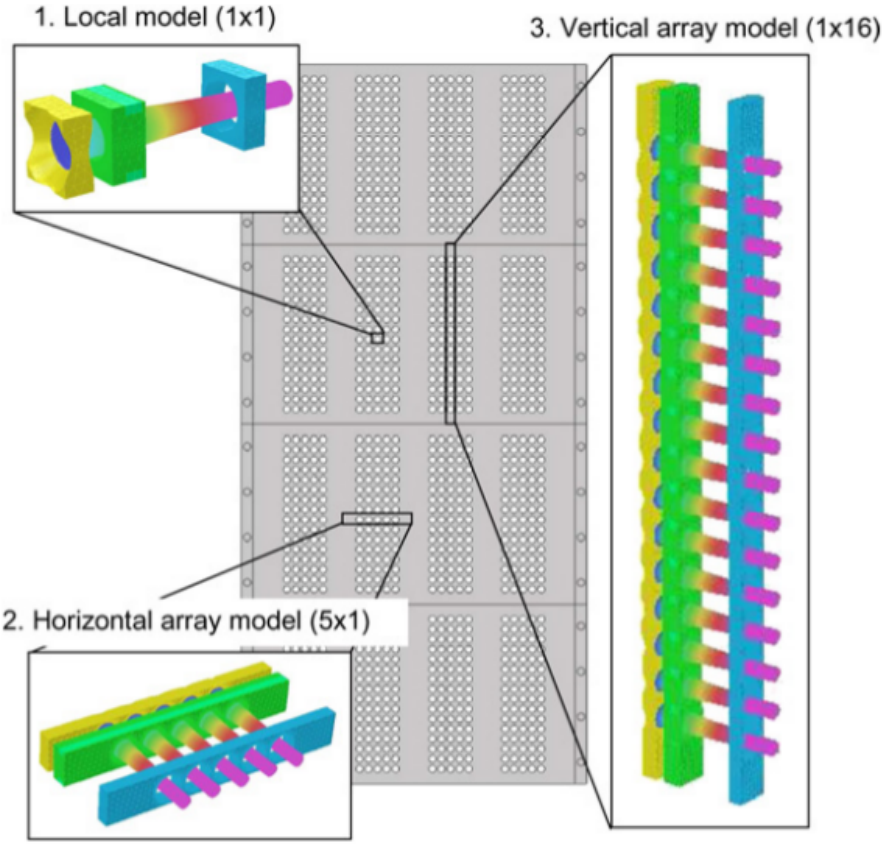


Figure 4.1: SPIDER beamlet arrangement[8]

Two different wire arrangements are simulated: the first one where the wire is in the vertical direction (in this case the beamlets depositing their power are 64: four groups of

16 beamlets), the second case is with the wire lying horizontally and hit by four groups of 5 beamlets. Two parameters were varied in the simulations: wire diameter and beamlet divergence. All the parameters and the values used in the simulations are listed in table 4.1.

| | |
|---|---|
| mesh | $1 \cdot 10^{-4}$ m |
| vertical wire length | 1.760 m |
| horizontal wire length | 0.820 m |
| Wire radius [mm]: | 0.1, 0.2, 0.3, 0.4, 0.5 |
| Divergence [mrad]: | 3.0, 5.0, 7.0, 10.0, 15.0 |
| Calorimeter position from the grid [m]: | 0.5 |
| Initial radius of the beamlet (at grid) [mm]: | 4.0 |

Table 4.1: Parameters of the simulation

Beamlets are represented as Gaussian functions centered in different positions along the wire and with the parameter $\sigma$ calculated as in eq.4.6:

$$\sigma_i = r_0 + \delta_i * L \tag{4.6}$$

where $\delta_i$ is the beamlet divergence, $L$ the distance between calorimeter and GG, $r_0$ the inital aperture of a beamlet; $\sigma$ along vertical and horizonal wire are assumed to be equal. As total power is distributed among several beamlets the integral under a bidimensional Gaussian function must be equal to the total power divided by the beamlet numerosity. This constraint allows to find the amplitude of the Gaussian (eq. 4.7)

$$\iint \frac{A^*}{2\pi\sigma\sigma} e^{-\frac{(x-\bar{x})^2}{2\sigma^2}} e^{-\frac{(y-\bar{y})^2}{2\sigma^2}} = A^* \tag{4.7}$$

where $A^*$ represent the power per beamlet ($A^* = \frac{780kW}{1280} = 610W$ see 4.2).
In the model also the neightbouring columns or rows of beamlets are considered: in this way it is possible to investigate the effect of high-divergence beamlets on the measuring wire. The whole energy flux is represented by eq.4.8

$$\begin{aligned} P_{flux} = A^* exp(-\frac{(x-x_{pos})^2}{2\sigma^2}) + \\ A^* exp(-\frac{(x-x_{pos})^2}{2\sigma^2}) exp(-\frac{(y_{beam'}-y_{pos})^2}{2\sigma^2}) + \\ A^* exp(-\frac{(x-x_{pos})^2}{2\sigma^2}) exp(-\frac{(y_{beam''}-y_{pos})^2}{2\sigma^2}) \end{aligned} \tag{4.8}$$

where $x_{pos}$ and $y_{pos}$ indicate the x-y coordinates of the wire; $y_{beam'}$ and $y_{beam''}$ represent the coordinates of the neightbouring column or row of beamlets.

## 4.2 Results of the simulations

It was decided to use a lower power beam due to the high temperatures reached on wire (above melting point). The power is scaled taking into account eq.1.9 The final used current is 15A with a voltage of 52 kV. The program was tested by imposing a thermal conductivity equal to 0: the main difference between different wire radii is the time by which thermal equilibrium is reached. The energy flux is described by a Gauss function

and each part of the wire reaches stationary conditions at different time. The model is a 200mm wire hit by a beamlet centered at 100mm. In the following figure are reported, depending on time, equilibration time at a distance of 125mm (fig.4.2 and fig.4.3). It is noticed that the greater the wire radius, the longer the time to reach equilibrium.

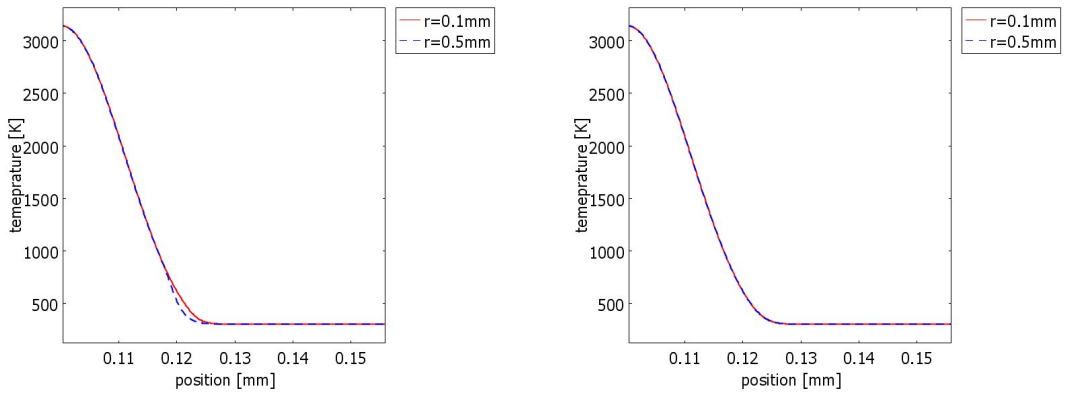


(a) *100s.* (b) *1000s and 10000s.*

Figure 4.2: test of the numerical model: temperature profile at different times

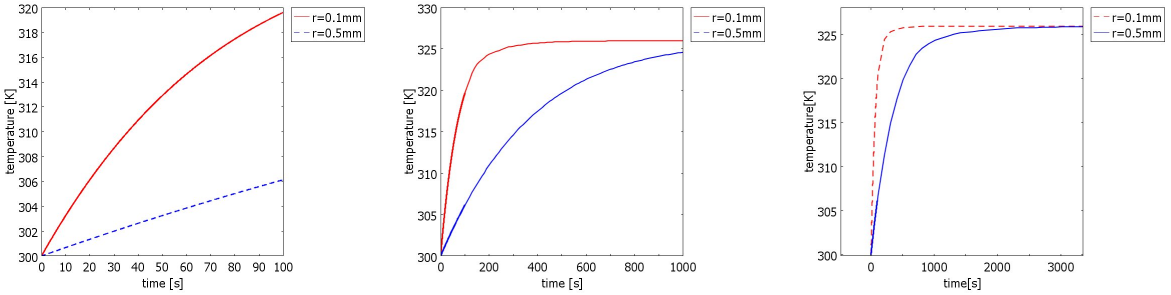


(a) *100s.* (b) *1000s.* (c) *10000s.*

Figure 4.3: Temperature profile at 125 cm after 100s,1000s,10000s (3mrad divergence)

Taking account of this phenomenon a simulation was performed using the parameter in eq.1.24 and eq.4.5 and for emissivity the eq.3.4. Results of analysis are reported below: fig.4.4,represent the temperature profile as a function of time.

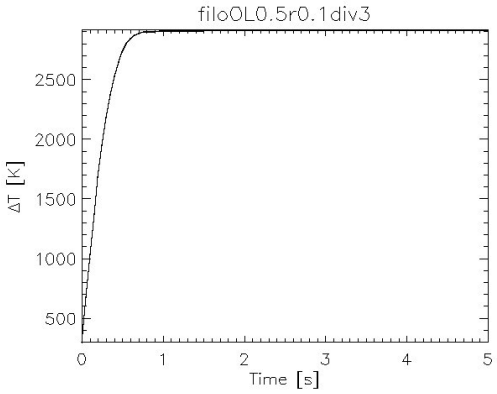


(a) *r=0.1mm.*

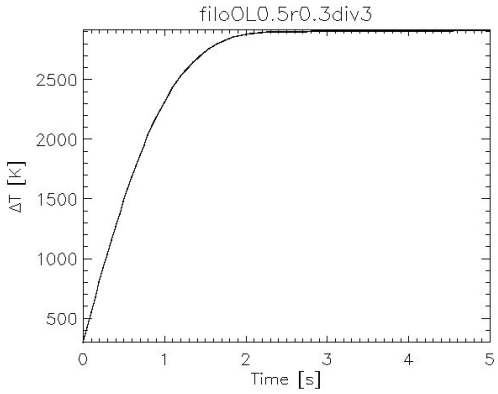


(b) *r=0.2mm.*

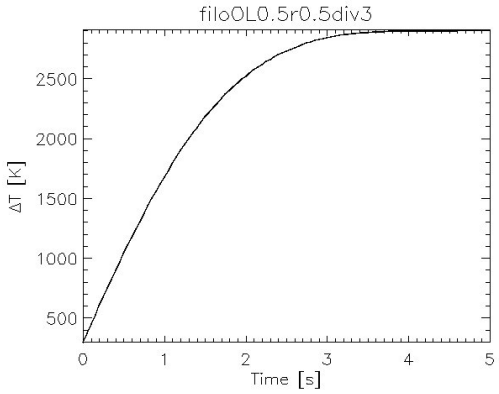


(c) *r=0.5mm.*

Figure 4.4: Temperature profile of different wires (divergence 3mrad)

As seen in tab.4.2 the $\tau$ parameter indicates the time in which the wire reaches the 61% of equilibrium temperature: to have a good spatial resolution of the beam profile measurement it is useful to choose a wire with a small radius.

| radius[mm] | $\tau$[s] |
|---|---|
| 0.1 | 0.2 |
| 0.2 | 0.45 |
| 0.3 | 0.65 |
| 0.4 | 0.92 |
| 0.5 | 1.15 |

Table 4.2: value of $\tau$ with respect to wires (divergence 3mrad)

Fig.4.5 reports, for the same wire radius, the temperature profile with different divergences.

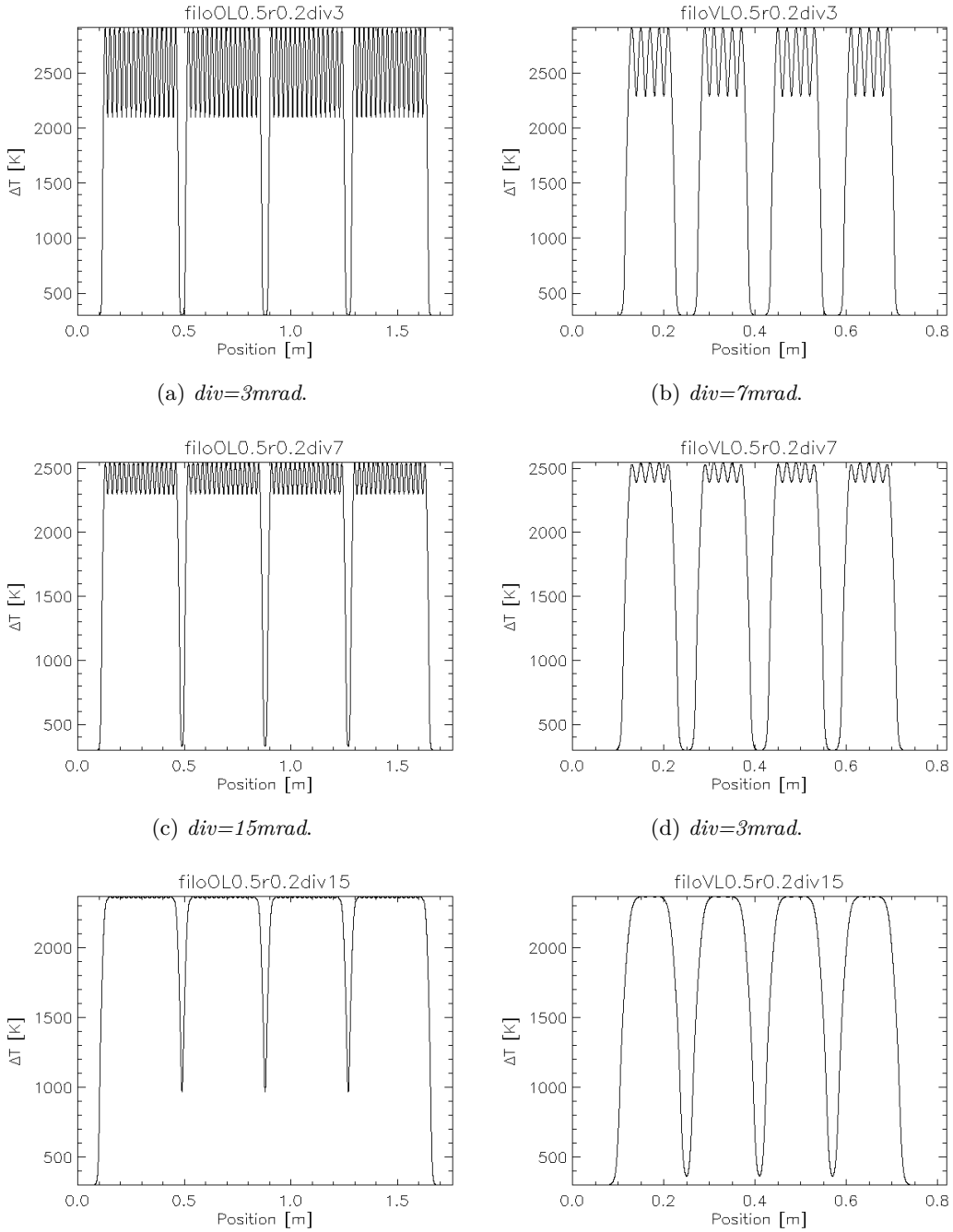


(a) *div=3mrad.* (b) *div=7mrad.*

(c) *div=15mrad.* (d) *div=3mrad.*

(e) *div=7mrad.* (f) *div=15mrad.*

Figure 4.5: Wire radius 0.2mm: vertical wire (first row) and horizonal wire (second row)

In fig.4.6 the normalizes emitted light $\sigma T^4$ is reported with different beamlet divergence.

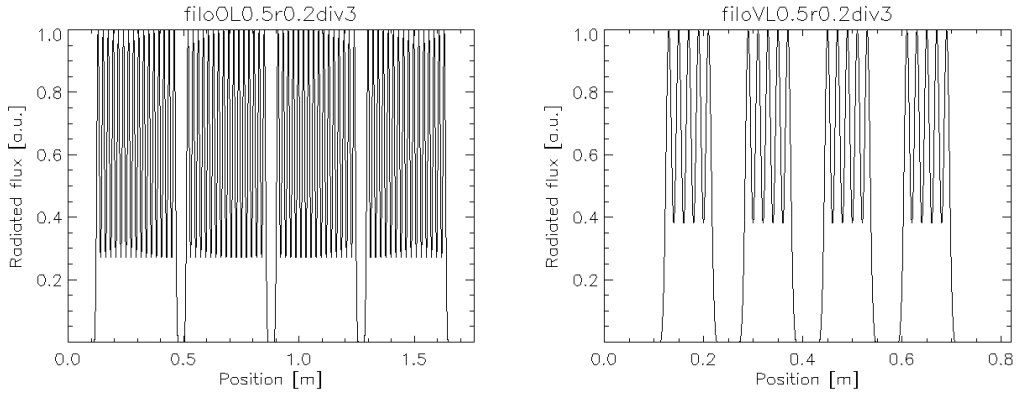


(a) *div=3mrad.*




(b) *div=3mrad.*

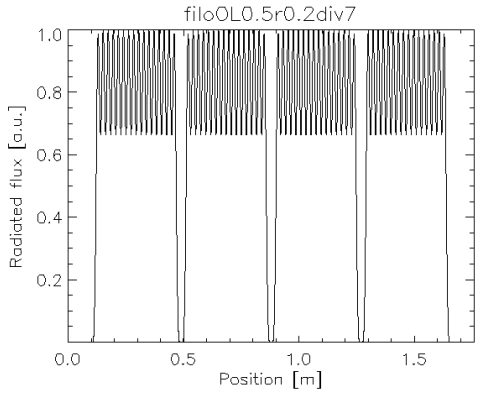


(c) *div=7mrad.*

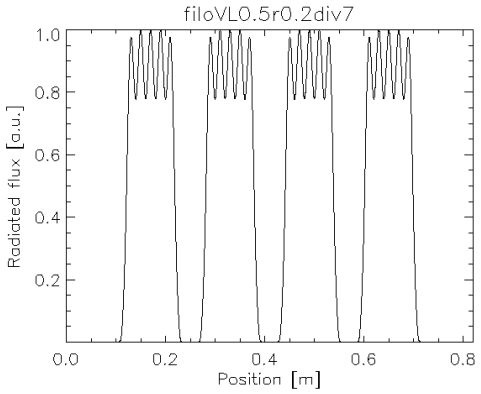


(d) *div=7mrad.*

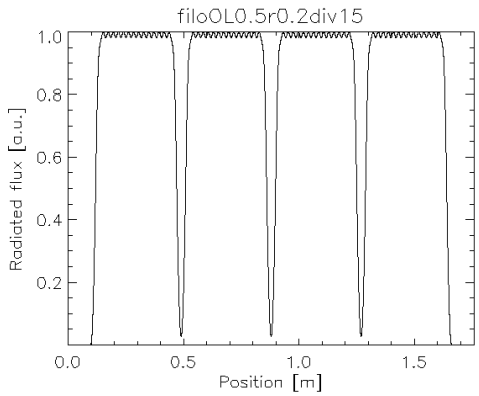


(e) *div=15mrad.*

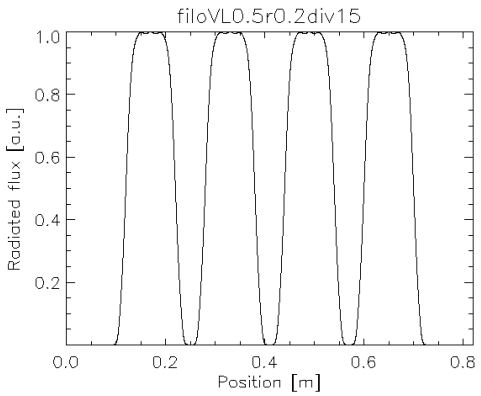


(f) *div=15mrad.*

Figure 4.6: Wire radius 0.2mm: vertical wire (first row) and horizonal wire (second row)

## 4.3 The effect of sputtering

The effect of sputtering Sputtering is a process whereby atoms are ejected from the surface of a target due to bombardment by energetic particles. To quantify the effect the sputtering yield $Y$ is introduced, which gives the number of ejected atoms per incident particle and depends on the material of the target, the energy and the type of the projectiles, the angle of incidence[11]. Considering the case of Tungsten hit by deuterium

and hydrogen and by approximating the surface as a plane (calculated area $S = 2rl$) it is possible to make a prediction on the erosion of the wires due to sputtering and, then, on the lifetime of the wires. The steady state current nominally expected provided by the beam source is of $355A/m^2$ for Hydrogen and $285A/m^2$ for Deuterium but considering the conditions discussed in section 4.2 these currents become $135A/m^2$ and $105A/m^2$ respectively (determined by eq.1.9). The wire lifetime is determined by calculating the number of sputtered particle per second (called $v$):

$$v = \frac{jY}{e}a^2 \tag{4.9}$$

where $a$ is the lattice constant. Then the lifetime in seconds is calculated by:

$$\frac{2r}{av} \tag{4.10}$$

results are reported in tab.4.3

| Particle type | r=0.1mm | r=0.2mm | r=0.3mm | r=0.4mm | r=0.5mm |
|---|---|---|---|---|---|
| **H** | $1.17\cdot 10^7$ | $2.33\cdot 10^7$ | $3.50\cdot 10^7$ | $4.67\cdot 10^7$ | $5.83\cdot 10^7$ |
| **D** | $4.72\cdot 10^6$ | $9.44\cdot 10^6$ | $1.42\cdot 10^7$ | $1.89\cdot 10^7$ | $2.36\cdot 10^7$ |

Table 4.3: lifetime in seconds

where the sputtering coefficient is 0.0013 for hydrogen and 0.004 for deuterium at an energy of 50 keV. In the assumed operational regime the calorimeter lifetime is about 3000 hours in case of hydrogen and 1300 hours in case of deuterium.
At such high temperature as the operational temperature of the wire calorimeter, also the effect of tungsten evaporation should taken into into consideration. Preliminary estimates along the same lines as for sputtering show that evaporation reduces the operational time with respect to sputtering alone

## 4.4 The camera point of view

As a starting point I consider the configuration of STRIKE[25] placing a camera at a distance of 2.5m from the calorimeter but using a CCD camera, with the same characteristics as the one used to capture images in this experiment, the Camera views is arranged perpendicularly to the diagnostic calorimeter. The CCD dectector is composed of 1920×1080 pixels of dimensions $5\mu m\times$ 5 $\mu m$ per pixel[19]. Below three cases are discussed:

- **One camera covers the whole calorimeter surface**: supposing the presence of a single camera focusing the whole calorimeter then the camera has to cover a surface of 800mm×1750mm (sum of the sizes of the calorimeter with the addition of a spacing of about 100mm to extremes) and the maximum resolution is given by:

$$\frac{800mm}{1080px} = 0.74mm/px \tag{4.11}$$

- **Two cameras cover each half of the calorimeter surface**: in case of using two different CCD cameras (one focused on the upper part and another focused on the lower part) the surface covered by a single camera is 800mm×1000mm (length

includes 2 beamlet groups anad a portion of the next one in order to correlate two images taken by the two cameras) the resolution in this case is given by:

$$\frac{1000mm}{1920px} = 0.52mm/px \tag{4.12}$$

- **One camera covers the surface of one beamlet group** this last case concerns the camera that covered only one beamlet group (with and additional spacing of about 100mm both vertically and horizontally) so the covered surface is aproximately 200mm×450mm. And the resolution is:

$$\frac{200mm}{1080px} = 0.19mm/px \tag{4.13}$$

These solutions are interchangeable and "modular". The next step is to choose the most suitable focal. The focal of a lens is defined as

$$\frac{1}{f} = \frac{1}{q} + \frac{1}{p} \tag{4.14}$$

where $f$ is the focal length, $p$ the distance between the object(in this case the calorimeter) $q$ the distance between the CCD detector and the lens. The magnification factor $M$ is defined as:

$$M = -\frac{q}{p} = \frac{f}{p-f} \tag{4.15}$$

it is to notice that for real images $M$ is negative. In cases discussed above $M$ is equal to the ratio between the pixel dimensions and the resolution. The final equation is:

$$M(p-f) = f \tag{4.16}$$

$$f = \frac{Mp}{M+1} \tag{4.17}$$

The lenses required for the cases above have a focal respectively of:

- $M = \frac{1}{148}$ and

$$f = \frac{2500mm}{148\left(\frac{1}{148}+1\right)} = 16.7mm \tag{4.18}$$

  commercial lens has a focal length of 16mm

- $M = \frac{1}{104}$ and

$$f = \frac{2500mm}{104\left(\frac{1}{104}+1\right)} = 23.8mm \tag{4.19}$$

  commercial lens has a focal length of 25mm: in this case it is necessary to displace the camera, taking into account mechanical costraints, at a distance of 2625mm from the wire calorimeter. Otherwise a lens with focal length of 16mm can be used wit a resulting resolution of $0.77mm/px$.

- $M = \frac{1}{38}$ and

$$f = \frac{2500mm}{38\left(\frac{1}{38}+1\right)} = 64.1mm \tag{4.20}$$

  commercial lens has a focal length of 50mm with a resulting resolution of $0.24mm/px$: in this case the image includes not only the beamlet group but also parts of neightbouring beamlet group.

The images will be affected by the presence of a non-homogeneous background radiation due to the presence of the $H_\alpha$ charge exchange spectral line.

## 4.5 Final consideration

To obtain a quantitative measure of the beamlet parameters it is necessary to calibrate the calorimeter: the calibration requires the passage of a well defined current through the wires and the acquisition of images of the calorimeter. In this way it creates a correspondence between power deposited in the wire and power emitted via radiation. Once obtained the calibration curve it must be reversed and used to derive the power deposited by the radiation emitted profile. On the basis of the discussion above, it can be deduced that a tungsten wire exposed to the SPIDER beam should exhibit a spatial profile allowing to resolve the beamlet size. To have a time resolution lower than 1s, wires with radius from 0.1mm to 0.3mm can be used; thicker wires will survive longer to sputtering and evaporation. A suitable two-dimensional arrangement of the wires should provide a proper imaging of the beam provided that either a sufficient number of cameras is employed (one per beamlet group) or a precise calibration is performed (in case of only one or two cameras, when the pixel size is larger than the wire). Since for wires 1.5m long thermal expansion is not negligible, it is necessary that a tension is applied to the wires; one possibility is by springs at the ends of the wires (like at IPP) or by attaching light weights at one end of the wires. Finally, to absolutely calibrate the whole system, a current should be drawn through the wires, so the tungsten calorimeter shall involve a current generator, a current vacuum feedthrough (rating is below 100A), a "multiplexing" system to distribute the current in vacuum to each wire (or to a significant fraction of the wires).All the aspects are to be investigated in detail.

# Chapter 5

# Conclusions

The optimisation of particle source neuatral beam injector used in nuclear fusion requires the characterisation of the beam features. Thistask can be accomplished by wire calorimeter. The present thesis gives a feasibility study of a tungsten wire calorimeter for the SPIDER experiment. The experiment shows a "baking" phenomenon at about 1300°K and after the experiment the surface looks shiny and bright. In the first part of the thesis the experiment on tungsten wires is designed in order to characterise wire parameter such as emissivity and thermal conduction: experimental results on tungsten wire show that conduction has a relevant role only for low temperature and that the emissivity is a constant. During the data collection it can be seen that wire radius and length change: this aspect is not included in data analysis but as a consequence the emissivity value is affected by a high error. The V-I curves shows a common trend and data analysis possess the reproducibility of measure events and, consequently, assure the validity of the measuring method. Moreover a possible CCD Camera is characterized: to acquire images two parameters are changed: integration time and gain. Integration time has a linear effect on pixel values over different orders of magnitude; the gain is also linear but it amplifies the background fluctuations and is correlated to the presence of unwanted effect like the presence of randomly arranged white pixels. At high integration time the background has not a fixed mean but presents lines of, on average, fixed value: this problem is overcomed by subtracting line by line the mean value of background in that line. The design of the W-wire calorimeter for SPIDER experiment device has been accomplished by taking into account ITER NBI requirements such as accurate beam divergence determination and extracted current density. The design, reported in this thesis, supposes a low power use and provides characteristics both for the camera and the tungsten wires. The idea is to use a diagnostic wire calorimeter to measure, via emitted radiation the beamlet deposited power: in order to use this instrument in a quantitative way a calibration is necessary. Calibration gives a correspondence between emitted radiation and deposited electric power: this correspondence is used to derive the power deposited by the beamlets from the measurement of emitted light. It should be noted that the calibration overcomes the problem of determining emissivity and thermal conductivity. The optimal wire radius is obtained considering the response time, the equilibrium temperature and the sputtering consumption. Camera characteristics have been defined starting from three possible configurations of camera with respect to the calorimeter, for each case it is calculated the focal of the associated lens: the best configuration among the three is the case of with focal value of. Several aspects have been analysed in this thesis: numerical simulations show that a wire calorimeter can be applied to the characterisation of the beam properties with a spatial resolution sufficient to resolve the beamlets. The considerations presented herein give the requirements of such a

calorimeter, in terms of wire thickness (taking into consideration the calorimeter lifetime), number, requirements and arrangement of the cameras employed to observe the emitted radiation. A calibration is required by passing a current in the wires. A more precise investigation is needed to design the supporting structure (including springs or weights to keep the wires straight despite thermal expansion) and the distribution system for the calibrating current, but the main result of the present work is that, at least for the first operations of SPIDER, when the beam power will be substantially lower than the design value, a wire calorimeter can be applied to the characterisation of the beam properties.

# Bibliography


[1] URL: http://www.efda.org/jet/.

[2] URL: https://fusion.gat.com/global/DIII-D.

[3] URL: http://www.lhd.nifs.ac.jp/en/.

[4] URL: http://www.ipp.mpg.de/ippcms/eng/pr/forschung/w7x/index.html.

[5] URL: http://www.ipp.mpg.de/.

[6] URL: http://www.hamamatsu.com/us/en/C10082CAH/index.html.

[7] F. J. Abellán et al. "The Stefan-Boltzmann constant obtained from the I-V curve of a bulb". In: *European Journal of Physics* 34 (2013), pp. 1221–1226.

[8] P. Agostinetti et al. "Physics and engineering design of the accelerator and electron dump for SPIDER". In: *Nuclear Fusion* 51 (2011), p. 063004.

[9] Aries. *Tungsten*. URL: http://aries.ucsd.edu/LIB/PROPS/PANOS/w.html.

[10] M. Bacal. "Physics aspects of negative ion sources". In: *Nuclear Fusion* 46.6 (2006), S250. URL: http://stacks.iop.org/0029-5515/46/i=6/a=S05.

[11] J. Bohdansky. "Sputtering". In: *Nuclear Fusion* Special issue (1984).

[12] I. Brown. *The physics and technology of ion sources*. 2003.

[13] M. Carlà. "Stefan-Boltzmann law for the tungsten filament of a light bulb: Revisiting the experiment". In: *American Journal of Physics* 81.7 (), pp. 512–517.

[14] Forsythe and Watson. "Resistance and Radiation of Tungsten as a Function of Temperature". In: *J.O.S.A.* 24 (Apr. 1934).

[15] Forsythe and Worthing. "The properties of tungsten and the characteristics of tungsten lamps". In: *The Astrophysical Journal* (1934).

[16] P. Franzen et al. "Progress of the Elise Test Facility: Results of Caesium Operation with low RF Power". In: *submitted to Nuclear Fusion* (2014).

[17] *Iter, the way to energy*. 2014. URL: http://www.iter.org/.

[18] H. A. Jones. "A temperature scale for tungsten". In: *Physical Review* 28 ().

[19] *KAI-02150 IMAGE SENSOR 1920 (H) X 1080 (V), INTERLINE CCD IMAGE SENSOR DEVICE PERFORMANCE SPECIFICATION*. Version REVISION 2.0 PS-0007. URL: www.truesenseimaging.com.

[20] M. Kikuchi, K. Lackner, and Q. M. Tran, eds. *Fusion Physics*. IAEA International Atomic Energy Agency.

[21] M. M. Bacal et al. "Basic processes of negative hydrogen ion production and destruction in sources and beams". In: *Rev. Sci. Instrum.* 46.6 (1996), p. 1138.

[22] R. Nocentini et al. "Beam diagnostic tools for the negative hydrogen ion source test facility ELISE". In: *Fusion Engineering and Design* 88 (2013), pp. 319–917.

[23] PLANSEE. *Tungsten (W)*. URL: http://www.plansee.com/en/Materials-Tungsten-403.htm.

[24] B. Prasad and R. Mascarenhas. "A laboratory experiment on the application of Stefan's law to tungsten filament electric lamps". In: *American Journal of Physics* 46 (), p. 420.

[25] A. Rizzolo et al. "Design and analyses of a one-dimensional CFC calorimeter for SPIDER beam characterisation". In: *Fus. Eng. Des.* 85 (2010), p. 2268.

[26] E. E. Salpeter. "Nuclear Reactions in the Stars. I. Proton-Proton Chain". In: *Phys. Rev.* 88 (3 1952), pp. 547–553. DOI: 10.1103/PhysRev.88.547. URL: http://link.aps.org/doi/10.1103/PhysRev.88.547.

[27] *SDK4 for Zelos cameras*. URL: www.kappa.de.

[28] P. Sonato et al. "Status of PRIMA, the test facility for ITER neutral beam injectors". In: *AIP Conf. Proc.* 1515 (2013), p. 549.

[29] P. Sonato et al. "The ITER full size plasma source device design". In: *Fusion Engineering and Design* 84 (2009), pp. 269–274.

[30] "Status of the ITER neutral beam injection system". In: *Rev. Sci. Instrum* ().

[31] P. Strehl. *Beam Instrumentation and Diagnostics*. Berlin: Springer, 2006.

[32] M. Zanini. "Analysis of a diagnostic potential of a wire calorimeter for characterization of particle beam". Bachelor. University of Padua.

**Ringraziamenti**

Ringrazio, in primo luogo, mia mamma Patrizia per avermi sostenuta e spronata ogni giorno, per le parole giuste al momento giusto, per la pazienza che dimostra ogni giorno. Ringrazio mio papà Maurizio per i tanti sorrisi, per l'allegria che riesce a comunicarmi, per la forza che dimostra ogni giorno davanti ai problemi. Ringrazio i miei nonni perchè ogni giorno mi spingono a studiare e per i tanti esempi di vita che mi hanno portato anno per anno. Ringrazio Andrea per il sostegno durante la mia carriera univeritaria e per la comprensione, soprattutto nell'ultimo periodo. Ringrazio Leonardo per i bellissimi momenti passati insieme, per l'interesse quotidiano, per l'infinita pazienza dimostrata in queste ultime settimane. Ringrazio tutti coloro, fortunatamente molti, che mi hanno aiutata e incoraggiata anche quando credevo di essere persa.
Non posso non ringraziare Dr. Gianluigi Serianni come relatore per l'aiuto, gli spunti e le idee che mi hanno aiutata giorno per giorno nel percorso verso la laurea, come persona per la passione nello svolgere il suo lavoro e per l'interesse dimostrato nei momenti di confronto e discussione. Ringrazio il Dr. Roberto Pasqualotto per il suo aiuto nello svolgimento della tesi, soprattutto per la parte di ottica. Ringrazio Daniele Fasolo per le interminabili ore passate con noi in laboratorio, per averci consentito di svolgere con tranquillità la tesi, per l'inestimabile esperienza nella difficile arte di far andare tutto al suo posto. Ringrazio Pierluigi Veltri per avermi aiutata, nelle ultime ore di disperazione, sia con il linguaggio MATLAB che con la simulazione COMSOL. Ringrazio il mio meccanico preferito, Vannino Cervaro, per la simpatia, la competenza e la pazienza nella costruzione dei pezzi per l'esperimento.
Venendo ai saluti più "profani" ringrazio ringrazio Laura, Lucia, Ludovica per le partite a carte, per le risate, per il casino; ringrazio di cuore i miei amici Luca, Pietro, Andrea per le indispensabili partite a carte del dopo-pranzo, per l'amicizia, per la buona volontà nel sopportarmi e per la leggerezza di ogni giorno passato insieme. Non posso dimenticare il mio amico "MM" Michele che mi da ogni giorno spunti per una battuta nuova e poi Lorenzo, per le parolacce e Federico, per l'aiuto offerto nel prendere in giro Michele.